Calibration Techniques for the Forward Hadron Calorimeter of the Compact Muon Solenoid

A THESIS
SUBMITTED TO THE FACULTY OF THE GRADUATE SCHOOL
OF THE UNIVERSITY OF MINNESOTA
BY

Perrie Leon Cole

IN PARTIAL FULFILLMENT OF THE REQUIREMENTS
FOR THE DEGREE OF
MASTER OF SCIENCE

Dr. Jeremiah Mans, Adviser

May 2010

Acknowledgements

First and foremost, I would like to thank my adviser, Dr. Jeremiah Mans, without whom none of this would have been possible. His endless patience and support throughout my research experience was truly inspirational. From answering minor technical questions to helping me set and meet writing deadlines, he has seen me through it all by teaching me the importance of asking for help while maintaining self-sufficiency. I would also like to thank Dr. Sinjini Sengupta for helping me greatly in my first year with CMS as I got my feet wet learning everything I needed to about CMS and the expectations for the calibration research. Thanks also to Nathan Mirman for his insights into the effects of position uncertainty in the HF. Other CMS collaboration members who were especially helpful to me over the past two years answering numerous technical questions include: Jason Haupt, Kevin Klapoetke and Abe DeBenedetti. Special thanks to everyone who read/proofread/offered suggestions on various drafts of this paper: Dr. Mans especially, but also Dr. Sengupta, Alex Gude, Ian Cole and Kristi Cronin. And a final thank you to my family and friends for their enduring support throughout my educational career and their constant encouragement to keep reaching for my dreams.

Dedication

This is dedicated to my mother who believes in me even when I do not believe in myself and who has taught me that it is possible to be critical of oneself without being unforgiving.

Abstract

The energy calibration of the various subdetectors in the Compact Muon Solenoid is necessary for the analyses to be done at the Large Hadron Collider. This is especially true of the Forward Hadron Calorimeter which endures the highest particle fluxes due to its high pseudorapidity. This paper discusses two possible calibration methods for the HF which take advantage of the high energy resolution of the Electromagnetic Calorimeter and the well separated products in Z→ee decays. The effectiveness of both methods will be discussed with respect to several scenarios of possible channel-to-channel correlations in pseudorapidity.

Contents

List of Tables

List of Figures

1 Introduction

This paper discusses two energy calibration procedures for the forward hadron calorimeter (HF) in the Compact Muon Solenoid (CMS) detector at the Large Hadron Collider (LHC). As the most forward subdetector in CMS, the HF receives the highest particle fluxes and is thus vital in some of the planned analyses with CMS. The Electromagnetic Calorimeter (ECAL) employs crystal calorimetry which provides excellent position and energy resolution. Additionally, the ECAL is also calibrated in situ using electrons whose momentum is measured by the tracker. The information from the tracker along with the carefully measured magentic field within the solenoid provide a good calibration for the ECAL. Since the HF is neither designed with this high energy resolution nor covering a portion of the tracker, a necessity exists for further calibration techniques.

Chapter 2 provides an introduction to the LHC accelerator and the CMS detector, as well as a more thorough discussion of the design of the HF. This chapter also gives a very basic overview of the primary research goals of the LHC and CMS.

Chapter 3 gives background information on the two calibration methods presented in this paper. This starts with a basic review of what a calibration is and how it can be used in the energy calibration of the HF. The previous calibrations done before the in situ calibration are discussed. A justification is also provided for the use of a Z→ee data sample for the purpose of calibration. The kinematics for calculating the predicted energy of an electron from this decay which is detected in the HF with the second electron detected in the ECAL is also derived in detail. This sets up the introduction of "fit" and "matrix" calibration techniques which depend on this predicted energy. And finally Chapter 3 includes a brief discussion on the effects of position uncertainty in HF on the measurement of the transverse momentum, p_T of the electron which ultimately limits the validity of the predicted energy of the HF electron.

Chapter 4 justifies the use of miscalibration scenarios as a method of stress testing our calibration methods. The event selection cuts for the ECAL and HF electrons in this decay are also discussed, largely in the context of reducing the effects of the background. The results from the two calibration techniques are presented and

compared to one another. From these results conclusions are drawn.

2 Detector

2.1 Design and Goals of LHC

The LHC is a 27 km circumference circular particle accelerator near the city of Geneva on the border of Switzerland and France. The majority of this circular structure is composed of superconducting magnets operating near absolute zero. These superconducting magnets include 1232 dipole magnets, each 15 m long, used to bend the beam, and 392 quadrupole magnets, 5-7 m in length, used to keep the beam in the pipe [1]. The dipole and quadrupole magnets are necessary to achieve collisions at the interaction points in the detectors (i.e. CMS, ATLAS), located at symmetric points around the circumference of the LHC (see fig. 1).

Previous experiments have successfully tested the Standard Model up to energies of ∼TeV. The first goal of the LHC is to further experimentally confirm the Standard Model at energies seven times this energy. Furthermore, the LHC seeks to understand electroweak symmetry breaking and investigate the Higgs mechanism. Alternatives that could be discovered at the LHC include supersymmetry or extra dimensions. In particular, the search for the Higgs Boson begins at masses above 114 GeV and includes such primary decay channels as $H \to \gamma\gamma, H \to bb$, or $H \to ZZ$. The $H \to ZZ \to 4l$ decay is ideal for Higgs Boson searches since the leptons should be easily identifiable. However the branching ratio for $Z \to ee$ is $\sim 3\%$, so this particular Higgs decay is rare. This rarity motivates our desire for accurate particle detection.

To further the achievement of these goals using proton-proton collisions, the design energy of the LHC is 7 TeV per proton beam, 14 TeV collision energy. The design luminosity is $10^{34}\text{cm}^{-2}\text{s}^{-1}$. For the initial years of the operation of the LHC, the beam energy will be set to 3.5 TeV per proton beam and the luminosity to less than $10^{33}\text{cm}^{-2}\text{s}^{-1}$ [1]. Aside from proton-proton collisions, heavy ion collisions will be studied at energies 30 times higher than experiments at other current accelerators.

2.2 A Note on Coordinate Conventions

The standard convention regarding coordinates in collider physics sets the positive z-axis as the beamline axis of the particle (as opposed to the antiparticle) with the

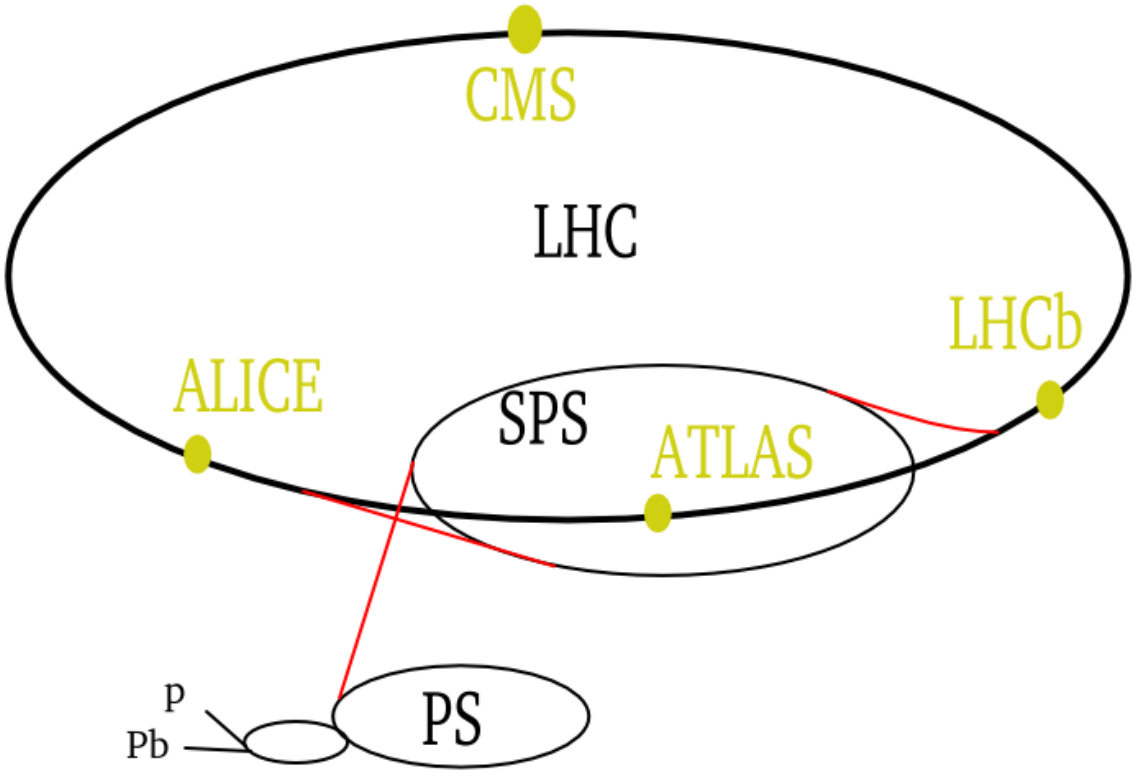

Figure 1: The LHC and the symmetric layout of the various detectors and accelerators

positive y-axis pointing vertically upward. However, in the LHC, the collision is proton-proton; therefore, the positive x-axis is defined as pointing radially inward toward the center of the LHC which, along with the upward facing positive y-axis, defines the beamline positive z-axis in accordance with a right-handed coordinate system. As usual, the azimuthal angle ϕ is measured with respect to the positive x-axis and the polar angle θ is measured with respect to the positive z-axis.

Pseudorapidity, defined as

$$\eta = -\ln(\tan[\theta/2]) \tag{1}$$

is conventionally used instead of the polar angle. The reason for this is that particle production is relatively constant as a function of pseudorapidity; therefore, pseudo-

rapidity will generally be used instead of polar angle in this paper.

2.3 Design of CMS

The CMS detector is, along with ATLAS, one of two general-purpose detectors for the LHC. The distinguishing feature of CMS, as the name implies, is the 3.8 T superconducting solenoid magnet which measures 13 m in length by 5.9 m inner diameter and contains all of the calorimetry [1] (see fig. 2). There are four detector levels within CMS, all of which are present in the central portion of the detector, $0 < |\eta| < 2.5$. Moving outward radially, the detector levels are: the tracker, the Electromagnetic Calorimeter (ECAL), the Hadron Calorimeter (HCAL), and the muon chambers. The tracker aids in the reconstruction of the position and momentum of high energy tracks of charged particles as they are bent in the strong magnetic field of CMS. The ECAL measures the position and energy of electrons and photons that deposit their energy as electromagnetic showers in the ECAL. The HCAL measures position and energy of hadrons that deposit their energy in the HCAL as electromagnetic showers. Finally, the muon chambers track the position and energy deposits of muons. This forms the last layer because muons are typically energetic enough to pass through several meters of iron without stopping. This detector level is necessary to ensure that position and energy data from muon events are not lost. Because muons are heavier than electrons, the radiation length for muons is higher than for electrons. While hadrons can be as energetic as muons, muons are generally longer lived than hadrons and don't have an interaction length characteristic of hadrons. Thus it becomes necessary to include an additional detector for energetic muons that live long enough to pass through HCAL.

For pseudorapidities ranging from $3.0 < |\eta| < 5.0$ the only detector level is in HCAL and is known as the Forward Calorimeter (HF), the design of which will be further explained in the next section.

2.4 HF Design

The HF portion of the HCAL is positioned 11.15 m from the interaction point of collision events [1] [2] and covers a pseudorapidity range from $3.0 < |\eta| < 5.0$. It aids

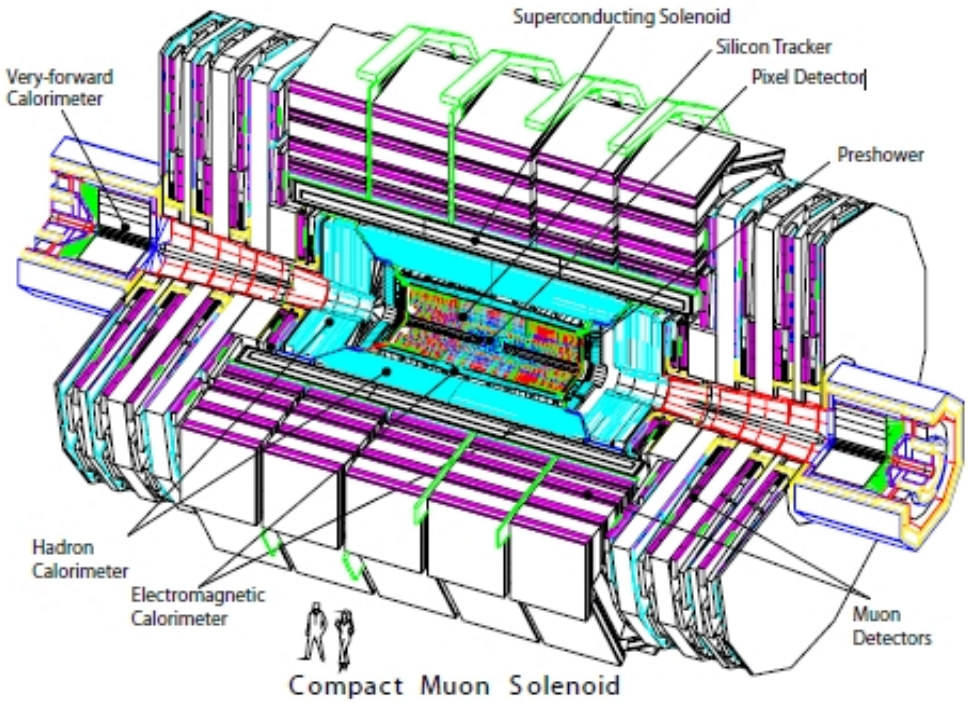

Figure 2: The Compact Muon Solenoid (CMS)

in the detection of energetic forward jets [2] and increases the hermeticity in measuring missing transverse energy which is necessary for some of the primary functions of CMS including SUSY and Standard Model Higgs particle studies. Thus the calibration of HF is vital for the successful accomplishment of these searches.

The large coverage of high pseudorapidities in the HF leads to much larger particle fluxes than in other portions of the detector. The average proton-proton interaction will deposit 760 GeV in the HF, as opposed to 100 GeV over the rest of the HCAL, with the highest fluxes at the largest pseudorapidities (smallest polar angles). This introduces one of the most significant design difficulties of HCAL: making the HF durable for such extreme radiation conditions over the expected lifetime (>10 years) of the LHC. The solution to the problem of making the HF durable for intense radiation doses is in the design of the active material. This active material consists of quartz fibers with fused-silica cores which are also polymer hard-clad [2], making

them especially radiation-hard and thus more durable to the extensive radiation that the detector will endure over nearly ten years. The signal carried by these quartz fibers is Cherenkov radiation from electrons which are produced in electromagnetic and hadronic showers. For example, a π^+ interacting in the HF will produce a shower of charged and neutral pions, which may decay into photons which initiate electromagnetic showers containing many electrons. Some of these electrons then produce Cherenkov radiation in the fibers if they impact above the critical angle, 71° [1] [2]. This radiation is then transmitted to the photomultiplier tube (PMT) photocathodes where the radiation is converted into a current which is converted to a digital signal at the readout boxes.

The fibers are shielded in the central portion of the HF by a polyethlene shielding [1] [2](see fig. 3). Polyethlene is chosen as the shielding material because of its utility in generating showers from neutral particles, such as neutrons, which would otherwise evade detection. The steel plug shielding shown in fig. 3 shields the light guides and PMTs from stray incoming particles coming from the beam.

The active absorber in the HF extends in the radial direction from 125 mm to 1300 mm above the beam line, and 1650 mm in the direction of the beam line. On the far end away from the interaction point, the quartz fibers in the absorber are connected to bundled fibers which are fed to air-core light guides which pass through a steel shielding (again for radiation hardness) which are read by PMTs in the readout boxes (See fig. 3) [2].

The HF calorimeter is composed of steel absorber plates which are 5 mm thick and contain grooves running parallel to the beam line spaced 5 mm apart from center to center. Two different lengths of quartz fibers are placed in these grooves in an alternating pattern. Half of the fibers run the entire length of the absorber (1650 mm); these are called the long fibers (L). The other half of the fibers are shorter starting 220 mm farther away (to the left in fig. 3) from the incoming beam than the long fibers; these are called the short fibers (S). This provides the distinction between signals caused by electromagnetic showers produced by electrons and photons, which tend to deposit most of their energy with the first 220 mm of the absorber [1] [2], and electromagnetic showers produced by hadrons. The long fibers will collect the entire signal (including showers from electrons and photons as well as hadrons), while

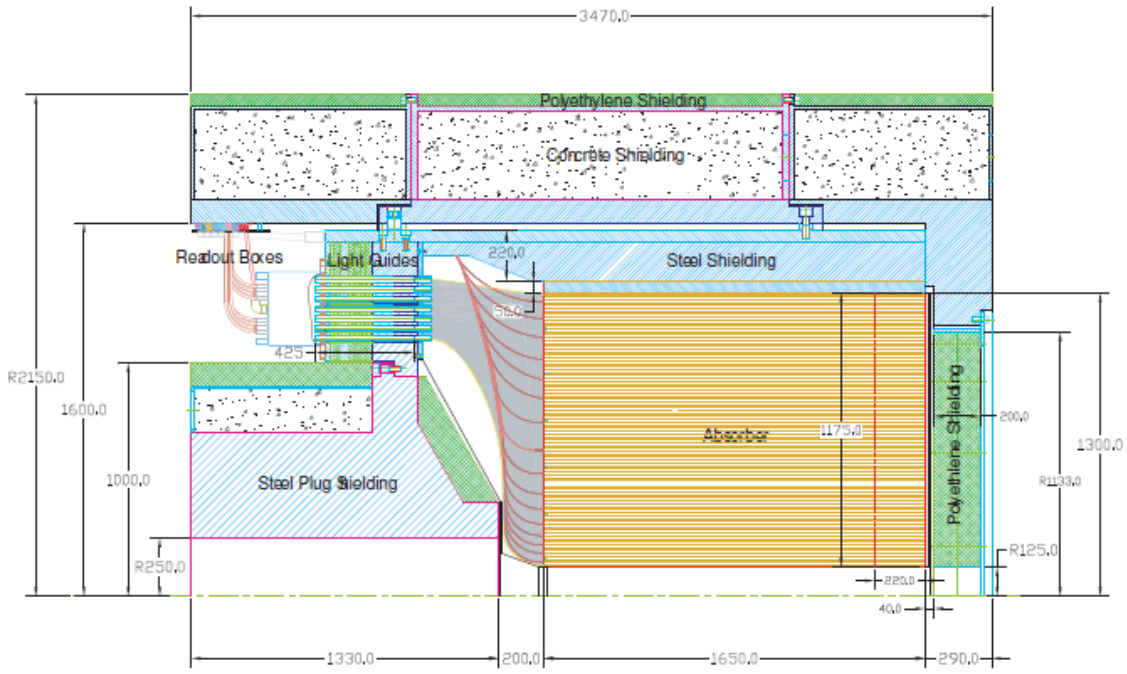

Figure 3: Side view of the HF detector. The interaction point is 11.15 m to the right. The vertical direction is the radial direction. The steel shielding around the absorber and light guides makes the detector radiation-hard against the exteme doses of radiation (coming from the left) the detector endures.

the short fibers will primarily see the electromagnetic showers from hadrons which enables hadron showers to be distinguished from electron or photon showers since the long and short fibers are connected to separate readout boxes.

The overall structure of the HF calorimeter is cylindrical, and this cylindrical structure is divided along the azimuthal direction into 18 wedges on each side of CMS (36 in all) of 20°. Each wedge is divided into 24 towers which group the fibers in each tower into the range of 0.175 x 0.175 ($\Delta\eta \times \Delta\phi$) with the exception of towers 12 and 13 which are closest to the beam line (see fig. 4) [1] [2]. Table 1 shows the size of each tower in HF in η and ϕ and the range of each ieta tower in η. Note that each tower has a corresponding index. This index correlates the tower labeled 1 in fig. 4 with the index 29, counting up to the tower labeled 13 in fig. 4, which has the

tower index 41. For the remainder of this paper, all towers will be referred to by tower index as opposed to the labeling convention used in fig. 4.

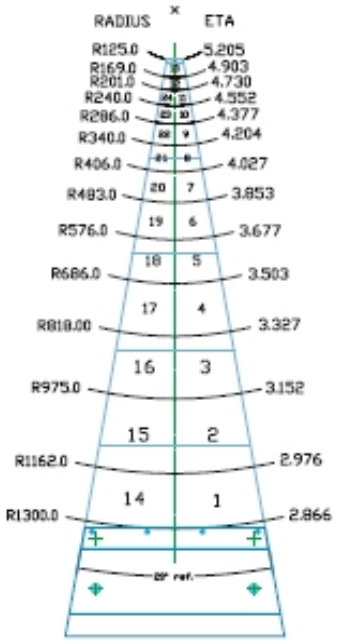

Figure 4: $r - \phi$ view of an HF wedge

Table 1: Specifications for HF wedge in η and ϕ

Tower Index	Low η	High η	Size in η	Size in ϕ
29	2.853	2.964	0.111	10°
30	2.964	3.139	0.175	10°
31	3.139	3.314	0.175	10°
32	3.314	3.489	0.175	10°
33	3.489	3.664	0.175	10°
34	3.664	3.839	0.175	10°
35	3.839	4.013	0.174	10°
36	4.013	4.191	0.178	10°
37	4.191	4.363	0.172	10°
38	4.363	4.538	0.175	10°
39	4.538	4.716	0.178	10°
40	4.716	4.889	0.173	20°
41	4.889	5.191	0.302	20°

3 Introduction to Calibration Methods

3.1 Concept/Methodology of Calibration

As described in the chapter 2, the signal determining the energy deposition of an electron in the HF is generated by Cherenkov radiation from the products in the resulting electromagnetic shower passing through the quartz fibers which transmit the Cherenkov radiation to the PMTs. Because Cherenkov radiation is generated only for light that enters the fibers at an angle greater than the critical angle, which is 71° for our quartz fibers, and because most of the energy loss in the electromagnetic showers occurs due to interactions with the iron absorber, most of the light from the electromagnetic shower will not be transmitted. Thus, there will be energy losses for which we need to compensate. This makes a calibration scheme for HF absolutely necessary.

As previously stated, the Cherenkov radiation generated for light entering the quartz fibers propagates through the fibers to the bundled fibers at the end of the absorber which are fed through air-core light guides (see fig. 3). The PMTs which observe the fibers then reads the buildup of current, which is then converted to a digital value in the readout boxes. Again, we are limiting ourselves to a study of the long fibers, or the electromagnetic showers, so we are only considering the amplitudes read by the readout box channels dedicated to the long fibers. This is the energy we would like to measure, so our calibration is intended to find the calibration constants that must by multiplied by the current measured in these fibers to get the deposited energy for electrons that are detected by these fibers. These constants have units of energy/charge and should take the form:

$$\epsilon = C(A - A_0) \tag{2}$$

where ϵ is the calibrated energy, C is a calibration constant, A is the strength of the signal current, and A_0 is a base current in the detector in the absence of collision particles.

3.2 State of Detector Before In Situ Calibration

A calibration has already been done on the HF wedges individually using a 5 mCi ^{60}Co source [2]. This was accomplished when gamma rays from this radioactive source generated Compton electrons that were able to generate Cherenkov light in the fibers being calibrated if they entered above the critical angle. The results from this test suggest that 5% calibration results were possible.

This could be compared to the results obtained using a test beam of known energy. This beam was focused on one ieta tower, and the signal measured in all towers, multiplied by their unknown respective calibration constants, were added linearly and set equal to the energy of the electrons in the beam. This was done for all 24 ieta towers in an HF wedge, leading to 24 linear combinations of amplitudes measured in a cell times the cell's calibration constants, all equal to the beam energy. These equations were solved for the 24 unknown calibration constants, and compared with the results using the radioactive source calibration technique.

The calibration constants obtained by the radioactive source calibration and the test beam calibration should, in theory, be equal to one another. In reality, there will be slight deviations. In this calibration study, the ratio of source constant to beam constant was taken for each ieta tower in a wedge, and the distributions of these ratios were plotted. The RMS values give us an idea of the quality of our calibration technique, and in this calibration suggest $\sim 5\%$ for long fibers and $\sim 7\%$ for short fibers [2].

While all of this has been done outside of the tunnel of the LHC, in situ calibration is still necessary since a chief goal in the calibration of all of the HCAL is to set an initial absolute energy scale and understand the detector response and uniformity. Also, conditions have changed since the previous calibration. The previous calibration was completed several years ago, above ground; the wedges have since been transported to CERN and lowered into the tunnel, etc. The channel-to-channel (where channel here is taken to mean ieta) calibration is considered to have a resolution of $\sim 12\%$ when all effects are taken into account.

The first in situ calibration will incorporate a phi-symmetry in the energy source which will be soft hadrons or jets. The reason for this choice of energy source is that

the in situ calibration needs to have large statistics and minimum bias in order to incorporate phi-symmetry. The large statistics available from these sources, in the absence of systematic errors, should give a nearly uniform reconstructed energy in each of the 36 iphi cells in a given ring of constant ieta. In reality, the reconstructed energies will not be uniform across all iphi cells, and thus correction factors need to be found via the following relation:

$$C_i = \frac{\sum_j \frac{\mu_j}{N}}{\mu_i} \tag{3}$$

Where C_i is the correction factor in iphi cell i, μ_i is the average energy in iphi cell i, and N is the number of iphi cells in the ring (in this case 36). The correction factor for a given iphi cell multiplied by the unadjusted average energy in that cell gives a uniform average energy for all iphi cells in the ring. And, unlike the ieta towers of a given iphi, the iphi cells in a ring of given ieta have uniform size, which should minimize errors due to position uncertainties in phi. However, any additive miscalibrations will eliminate our phi-symmetry. This paper discusses an in situ calibration assuming ϕ-symmetry, and determining calibration constants for channels in η (ieta).

3.3 The Signal Z Boson

The signal used for this calibration is $Z \to ee$. To understand why this signal is of particular interest to us, it is necessary to review the attributes of the Z boson. The electrically neutral Z boson is one of three massive vector bosons which mediate the Weak Force. It is the most massive of the vector bosons and has one of the most accurately measured masses of any particle. The Particle Data Group gives the mass of the Z boson as 91.1876±0.0021 GeV [3]. In the LHC, the production mechanism for the Z boson is $pp \to Z + X$.

There are many reasons why the Z boson is particularly well-suited for this analysis. First of all, we know the mass of the Z boson very accurately and we know that it is the most massive of the massive vector bosons, which means that the decay particles will generally be very energetic. The large mass of the Z boson is helpful because the decay is to two well separated decay particles. This means that there will be more decay events to two electrons with one electron with a large enough

transverse momentum component that it will end up in the ECAL, allowing us to take advantage of the position and energy resolution of the crystal calorimetry in the ECAL, with the second electron absorbed in the HF. While it might be possible to isolate Z decays which involve jets, such an analysis would be complicated. However, other calibration techniques have sought to calibrate the HF by balancing photons against jets. Even though the branching ratio of $Z \rightarrow ee$ is roughly 3%, electron decay products are easily identifiable, thus making this an ideal decay mode to use for our calibration.

3.4 Fakes and Backgrounds

For accurate electron detection, it is necessary to distinguish true electrons from jets that can look like electrons to the detector. Since the electrons are highly separated in the decay of the Z boson, we can suppress fake electrons by making tight isolation cuts in the tracker, ECAL, and HCAL which only consider particle hits with a transverse momentum larger than a certain threshold within a cone for each of these detector levels [4] [5]. Furthermore, electron identification cuts can be made on the ECAL electron which suppress the jet background; these cuts will be discussed further in the next chapter. The distinction between long and short fibers in the HF helps us identify true electrons from fake electrons, since electrons will deposit most of their energy in the short fibers and jets, being hadronic, will deposit energy in both the short and long fibers. There are futher identification cuts in the HF which distinguish electrons from jets; these will be discussed in the next chapter. Even with these isolation and identification cuts, the lack of tracker coverage for the HF electron leads to larger backgrounds for Z→ee events with one ECAL and one HF electron than if we had used two ECAL electrons; this is mostly due to QCD events. Identification cuts will be discussed in chapter 4 and will be optimized to reduce the effects of the background.

3.5 Derivation of Predicted Energy of HF Electron

Our analysis is for $Z \rightarrow ee$ events in which one electron is detected in the ECAL and one in the HF. As discussed previously, the energy and position resolution made

possible by the crystal calorimetry of the ECAL gives reconstructed position and energy for the ECAL electron near truth level. The goal is to find a prediction equation for the energy of the HF electron. We will now review the kinematics necessary to find the energy of the HF electron given its position, the mass of the Z boson, and the energy and position of the ECAL electron. In the center of mass frame of the Z boson, the 4-momentum is:

$$(m_Z, \vec{0}) = (E_E + E_H, \vec{p_E} + \vec{p_H}) \tag{4}$$

Therefore:

$$\begin{aligned} s &= m_Z^2 = (E_E + E_H)^2 - (\vec{p}_E + \vec{p}_H)^2 && (5)\\ &= (E_E^2 - |\vec{p}_E|^2) + (E_H^2 - |\vec{p}_H|^2) + 2E_E E_H - 2\vec{p}_E \cdot \vec{p}_H && (6)\\ &= 2m_e^2 + 2E_E E_H - 2|\vec{p}_E||\vec{p}_H|\cos\theta && (7) \end{aligned}$$

where θ is the opening angle between the two electrons. The energies of all the electrons that pass our cuts are $\gg$ MeV. Therefore, $E_E \sim |\vec{p}_E|$ and $E_H \sim |\vec{p}_H|$. Therefore:

$$m_Z^2 = 2m_e^2 + 2E_E E_H(1 - \cos\theta) \tag{8}$$

It follows from the previous assumption that we can approximate $m_e \sim 0$. So, solving for E_H:

$$E_H = \frac{m_Z^2}{2E_E(1 - \cos\theta)} \tag{9}$$

Let us now solve for $\cos\theta$:

$$\cos\theta = \frac{\vec{p}_E \cdot \vec{p}_H}{|\vec{p}_E||\vec{p}_H|} \tag{10}$$

To solve the dot products for the momenta, we identify the form for p_x, p_y, p_z in terms of the azimuthal angle and pseudorapidity:

$$p_x = E\frac{\cos\phi}{\cosh\eta} \tag{11}$$

$$p_y = E\frac{\sin\phi}{\cosh\eta} \tag{12}$$

$$p_z = E\tanh\eta \tag{13}$$

Inserting these momenta vectors in our previously found equation for $\cos\theta$ gives:

$$\cos\theta = \frac{E_E E_H(\frac{\cos\phi_E\cos\phi_H+\sin\phi_E\sin\phi_H}{\cosh\eta_E\cosh\eta_H} + \tanh\eta_E\tanh\eta_H)}{E_E E_H(\sqrt{\frac{\cos^2\phi_E+\sin^2\phi_E}{\cosh^2\eta_E} + \tanh^2\eta_E})(\sqrt{\frac{\cos^2\phi_H+sin^2\phi_H}{\cosh^2\eta_H} + \tanh^2\eta_H})} \tag{14}$$

Using the relations $\cos\phi_E\cos\phi_H + \sin\phi_E\sin\phi_H = \cos(\phi_E - \phi_H)$ and $\cos^2\phi + \sin^2\phi = 1$ we can simplify:

$$\cos\theta = \frac{\frac{\cos(\phi_E-\phi_H)+\sinh\eta_E\sinh\eta_H}{\cosh\eta_E\cosh\eta_H}}{\frac{1}{\cosh\eta_E\cosh\eta_H}(\sqrt{1+\sinh^2\eta_E})(\sqrt{1+\sinh^2\eta_H})} \tag{15}$$

Using the relation $1 + \sinh^2\eta = \cosh^2\eta$:

$$\cos\theta = \frac{\cos(\phi_E - \phi_H) + \sinh\eta_E\sinh\eta_H}{\cosh\eta_E\cosh\eta_H} \tag{16}$$

Substituting our solution for $\cos\theta$, our solution for E_H:

$$E_H = \frac{m_Z^2}{2E_E(1 - \frac{\cos(\phi_E-\phi_H)+\sinh\eta_E\sinh\eta_H}{\cosh\eta_E\cosh\eta_H})} \tag{17}$$

$$= \frac{m_Z^2\cosh\eta_E\cosh\eta_H}{2E_E(\cosh\eta_E\cosh\eta_H - \sinh\eta_E\sinh\eta_H - \cos(\phi_E - \phi_H))} \tag{18}$$

Finally,

$$E_H = \frac{m_Z^2\cosh\eta_E\cosh\eta_H}{2E_E(\cosh(\eta_E - \eta_H) - \cos(\phi_E - \phi_H))} \tag{19}$$

Note that while the energy of the HF electron is dependent on Z mass, as well as the position and energy of the ECAL electron, all of which we consider to be well known, it is also dependent on the position of the HF electron which may also be subject to biases.

3.6 Using Energy Prediction Directly

The energy of the HF electron found in the previous section, E_H, is the $E_{predicted}$ for calibration purposes. The reconstructed energy of the HF electron, E_{reco}, $= C_1 A$, where C_1 is a calibration constant and A is a rough energy. To get closer agreement between E_{reco} and E_{pred}, a second calibration constant C_2 may be multiplied to E_{reco}. Therefore, the new energy afer calibration will be $C_2 E_{reco}$ or $C_2[C_1 A]$. This process can be iterated, yielding calibration constants, $C_3, C_4...$, which will bring the calibrated reconstructed energy into closer agreement with the predicted energy. If the idea behind the calibration is to achieve greater agreement between E_{reco} and E_{pred}, we can get a preliminary calibration by taking the ratio of E_{reco} to E_{pred} (see fig. 5). This "fit" technique can be iterated achieving ratios closer to one. This "fit" technique was performed preceeding the "matrix" technique which is explained in the next section. Each process can be repeated. Throughout all of this, it is important to keep in mind that we have assumed that the ieta channels are independent of one another and thus require individual calibration constants.

3.7 Matrix Calibration

A matrix calibration technique can be used to determine calibration constants for multiple channels for the amplitude of a target quantity in each channel for each event. Since this analysis assumes phi-symmetry, the channels will be the ieta towers. For the purposes of this calibration, we are taking the amplitude as the reconstructed energy of the HF electron in each ieta tower for each event. Let C_i be the calibration constant for the i-th channel, A_i^d be the amplitude of the target quantity measured in the i-th channel for the d-th event, and E^d be the expected value of the target quantity for the d-th event. In this calibration, the expected value is derived from the prediction equation for the HF electron energy found in the previous section (using

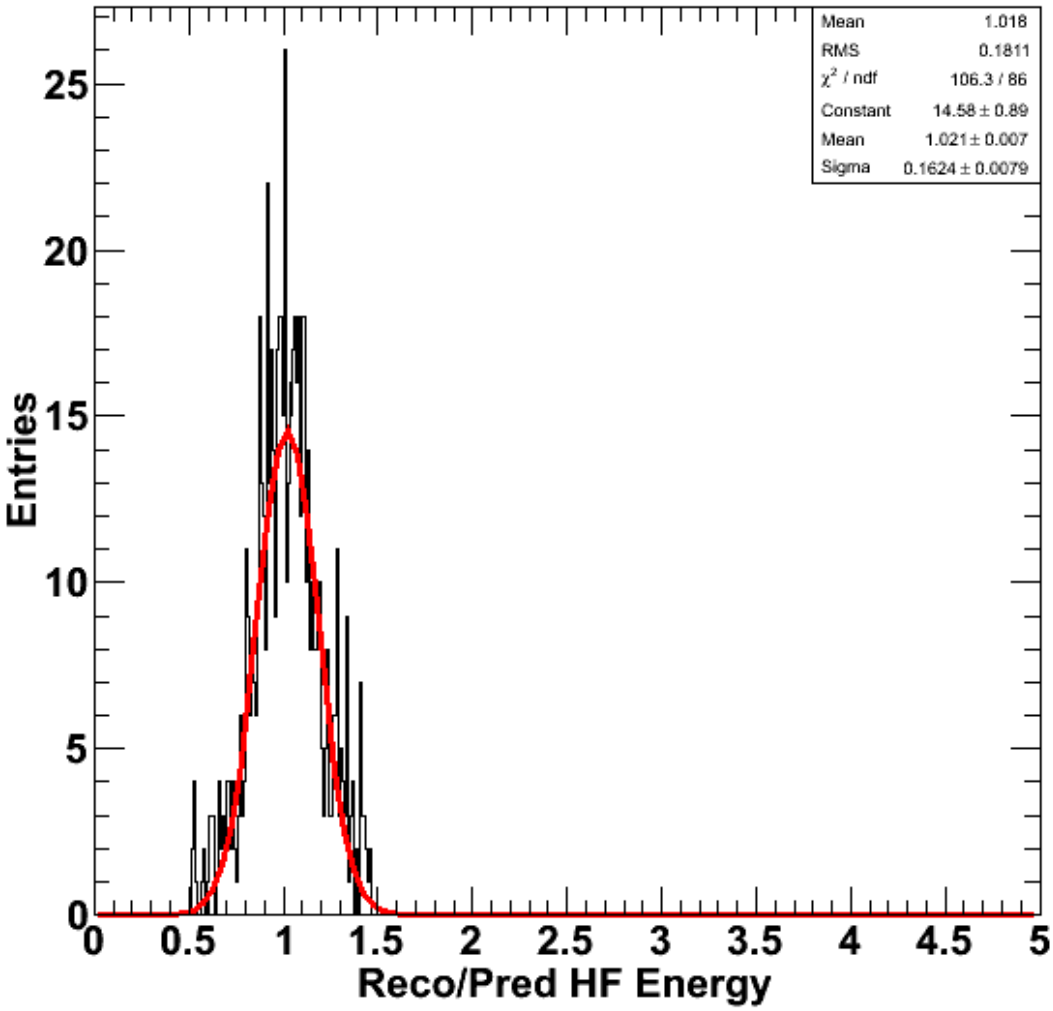

Figure 5: A sample histogram of ratio of Reconstructed to Predicted HF electron energy in ieta tower 33

the known Z mass as well as the reconstructed values for postion/energy of the ECAL electron and position of the HF electron). Chi-squared is then given by:

$$\chi^2 = \sum_d \frac{[\sum_i C_i A_i^d - E^d]^2}{\sigma_d^2} \quad (20)$$

$$= \sum_d \frac{[\sum_i C_i A_i^d]^2 - 2E^d \sum_i C_i A_i^d + (E^d)^2}{\sigma_d^2} \quad (21)$$

Calibration constants are chosen such that the chi-squared is minimized. Therefore:

$$\frac{d\chi^2}{dC_j} = 0 \quad (22)$$

$$\frac{d}{dC_j}[\sum_d \frac{[\sum_i C_i A_i^d]^2 - 2E^d \sum_i C_i A_i^d + (E^d)^2}{\sigma_d^2}] = 0 \quad (23)$$

Let us expand the square of the sum over i:

$$[\sum_i C_i A_i^d]^2 = (\sum_i C_i A_i^d)(\sum_k C_k A_k^d) \quad (24)$$

$$= \sum_i \sum_k C_i C_k A_i^d A_k^d \quad (25)$$

$$\frac{d}{dC_j}[\sum_i C_i A_i^d]^2 = 2\sum_i C_i A_i^d A_j^d \quad (26)$$

The derivative of the chi-squared with respect to the calibration constants then becomes:

$$0 = \sum_d \frac{2\sum_i C_i A_i^d A_j^d - 2E^d A_j^d}{\sigma_d^2} \quad (27)$$

$$= \sum_d \frac{\sum_i C_i A_i^d A_j^d}{\sigma_d^2} - \sum_d \frac{E^d A_j^d}{\sigma_d^2} \quad (28)$$

$$= \sum_i C_i \frac{\sum_d A_i^d A_j^d}{\sigma_d^2} - \sum_d \frac{E^d A_j^d}{\sigma_d^2} \quad (29)$$

$$\sum_d \frac{E^d A_j^d}{\sigma_d^2} = \sum_i C_i [\sum_d \frac{A_i^d A_j^d}{\sigma_d^2}] \quad (30)$$

This equation will be used to find the calibration constant for each channel (ieta tower). Let us simplify this expression this expression with a few definitions:

$$M_{ij} = \sum_d \frac{A_i^d A_j^d}{\sigma_d^2} \quad (31)$$

and

$$b_j = \sum_d \frac{E^d A_j^d}{\sigma_d^2} \quad (32)$$

Therefore, (30) can be simplified and rewritten as:

$$b_j = \sum_i C_i M_{ij} \quad (33)$$

This can also be represented in matrix form as:

$$\vec{b} = M\vec{C} \quad (34)$$

We can solve this for $\vec{C}$ through matrix inversion

$$M^{-1}\vec{b} = M^{-1}M\vec{C} \quad (35)$$

$$\vec{C} = M^{-1}\vec{b} \quad (36)$$

For any given event, the energy of the HF electron is taken in a cluster with one additional ieta tower on either side of the seed tower where the vast majority of the energy of the electron is deposited. Therefore, energy of the HF electron is only considered for three ieta towers for each event which means the matrix M is a symmetric matrix with most of the off-diagonal elements equal to zero, and only three elements of the vector $\vec{b}$ incremeted for each event.

3.8 Effects of Position Uncertainty in HF

Up to this point, we have stressed the importance of having a calibration of energy in the HF. For this purpose we've discovered that it is beneficial to look at Z→ee events with one electron going to the ECAL and one to the HF. The reason we set this condition is that the crystal calorimetry of the ECAL gives position and energy measurements for electrons near truth level. Utilizing the predicted energy equation of the HF electron found previously can, therefore, yield an energy which is, in principal, close to truth level. However, this equation has limited predictive validity because the position resolution in the HF cannot match that in the ECAL and since the predicted energy equation is dependent on the position of the HF electron, there is a degree of uncertainty in our energy prediction. It is prudent for us, then, to quantitatively examine the effects of a translation of position of the HF electron measurement.

The transverse momentum, p_T, is defined as:

$$p_T = \frac{p}{\cosh \eta} \tag{37}$$

Using the relations $\tan\theta = 1/\sinh\eta$ and $\cosh^2\eta = 1 + \sinh^2\eta$ we find:

$$p_T = \frac{p}{[1 + (\frac{z}{r})^2]^{1/2}} \tag{38}$$

If we keep y, z and p constant and let x → x' = x +δx, then:

$$p'_T/p_T = [\frac{1 + (\frac{z}{r})^2}{1 + (\frac{z}{r'})^2}]^{1/2} \tag{39}$$

where $r^2 = x^2+y^2$ and $r'^2 = x'^2+y^2$ and:

$$x = r\cos\phi = z\frac{\cos\phi}{\sinh\eta} \tag{40}$$

$$y = r\sin\phi = z\frac{\sin\phi}{\sinh\eta} \tag{41}$$

Therefore:

$$(\frac{z}{r'})^2 = \frac{z^2}{x'^2+y^2} = \frac{z^2}{x^2+2x(\delta x)+(\delta x)^2+y^2} \quad (42)$$

$$= \frac{(\frac{z}{x})^2}{z^2(\frac{\sinh^2\eta}{\sin^2\phi})+1+2(\frac{\delta x}{x})+(\frac{\delta x}{x})^2} \quad (43)$$

$$= \frac{\frac{\sinh^2\eta}{\cos^2\phi}}{1+2(\frac{\sinh\eta}{\cos\phi})(\frac{\delta x}{z})+(\frac{\sinh\eta}{\cos\phi})^2(\frac{\delta x}{z})^2+\tan^2\phi} \quad (44)$$

$$= \frac{\sinh^2\eta}{1+2\sinh\eta\cos\phi(\frac{\delta x}{z})+\sinh^2\eta(\frac{\delta x}{z})^2} \quad (45)$$

This leads to:

$$\frac{p'_T}{p_T} = [\frac{1+\sinh^2\eta}{1+\Lambda^2\sinh^2\eta}]^{1/2} \quad (46)$$

where

$$\Lambda = [1+2\sinh\eta\cos\phi(\frac{\delta x}{z})+\sinh^2\eta(\frac{\delta x}{z})^2]^{-1/2} \quad (47)$$

At the high η values in the HF the ratio of translated transverse momentum to transverse momentum reduces to $\sim \Lambda^{-1}$ This equation holds for translations in the y-direction as well. Interestingly, a misalignment of the HF would also break the phi symmetry discussed in 3.3. Thus the calibration techniques to be discussed may serve the additional purpose of providing a cross check on the alignment of the HF.

4 Calibration

4.1 Introduction of Miscalibration Scenarios

As explained previously, a portion of the electromagnetic shower generated by the electron in the HF produces Cherenkov radiation in the quartz fibers which produce a current in the PMTs which is carried to the readout boxes where it is read as an energy. There is no manual calibration at this point, so we call this the base case. Presumably, since the wedges of HF have already been calibrated off site, any miscalibration in the ieta towers should be a constant that holds for each tower. However, by manually applying a miscalibration factor to the energies read in each ieta tower, we can "stress test" our calibration methodology against large miscalibration differences between adjacent ieta towers. These miscalibration constants highlight a varying correlation between channels following distinct patterns. For our purposes, we introduce five miscalibration scenarios with miscalibration constants varying between 80% to 120% (of the ratio E_{reco}/E_{pred}): linear, inverse linear, sinusoidal, sawtooth, and random (see figs. 6 to 10). These miscalibration scenarios provide a unique set of challenges that highlight the effects of different correlations between adjacent channels.

4.2 Event Selection

Each event has to have two electrons (one in ECAL ($\eta < 3$) and one in HF ($3 < \eta < 5$)), where the ECAL elctron has to have a transverse energy greater than 15 GeV, and the HF electron a transverse energy greater than 10 GeV. The trigger for this process is a high p_T isolated electron. The ECAL electron is required to be within the tracking region, which requires isolation cuts in each level of the detector (tracker, ECAL, and HCAL). The isolation variables are determined by summing the transverse momentum for all tracks or hits within a cone, excluding some inner region. It should be mentioned that the isolation cuts vary depending on the data sample. The cones defining the tracking regions within the subdetectors are: $0.015 < \Delta R < 0.3$ for the tracker, $0.070 < \Delta R < 0.4$ for the ECAL Endcap (we choose to use the Endcap isolation cut instead of the Barrel isolation since this cut tends to be tighter), and

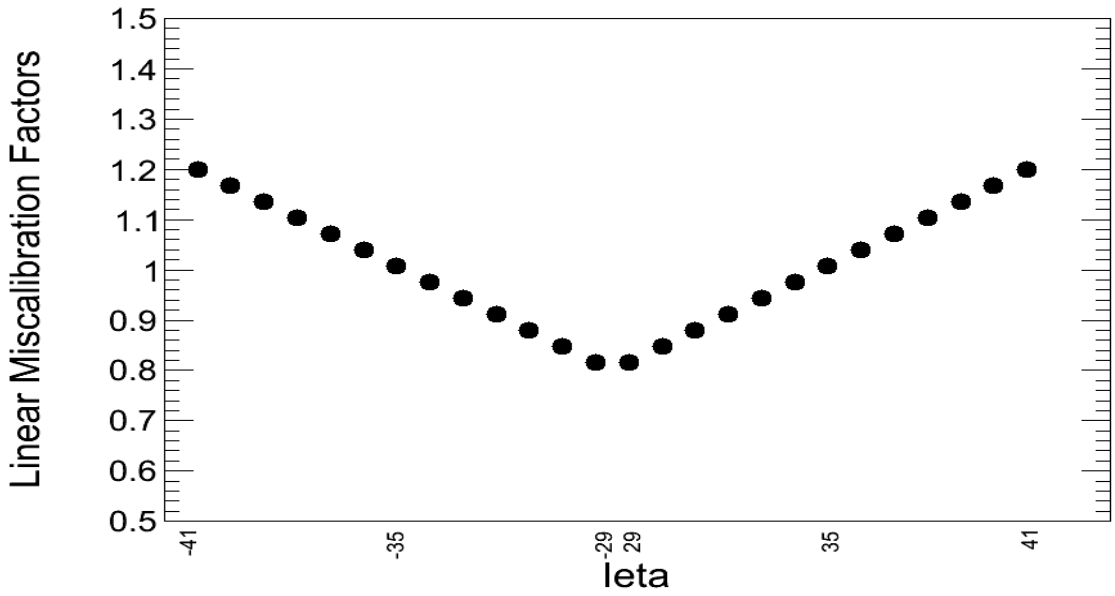

Figure 6: Linear miscalibration scenario

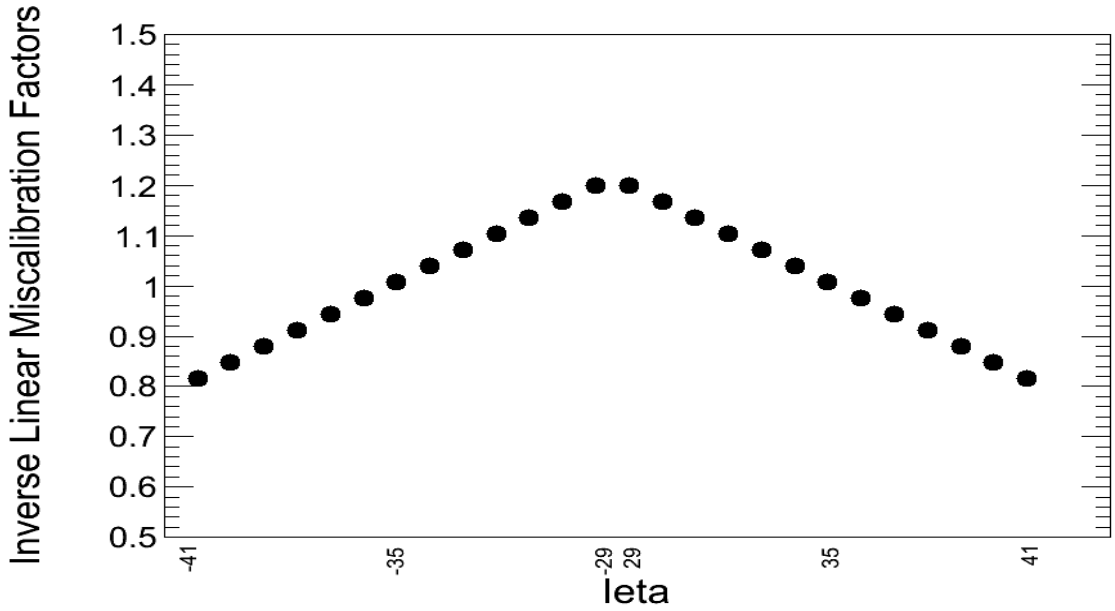

Figure 7: Inverse linear miscalibration scenario

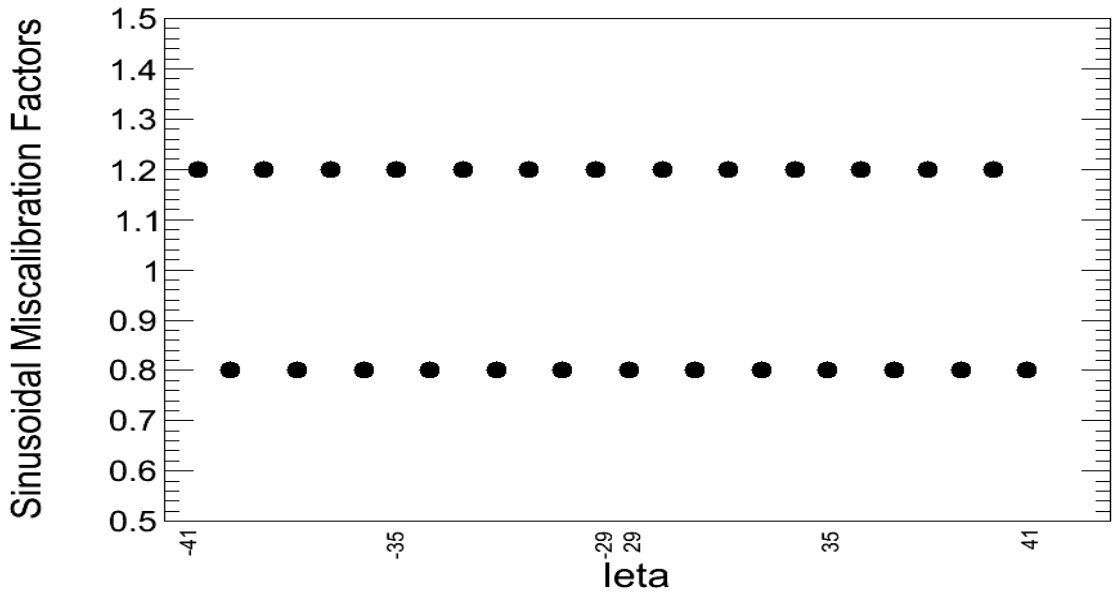

Figure 8: Sinusoidal miscalibration scenario

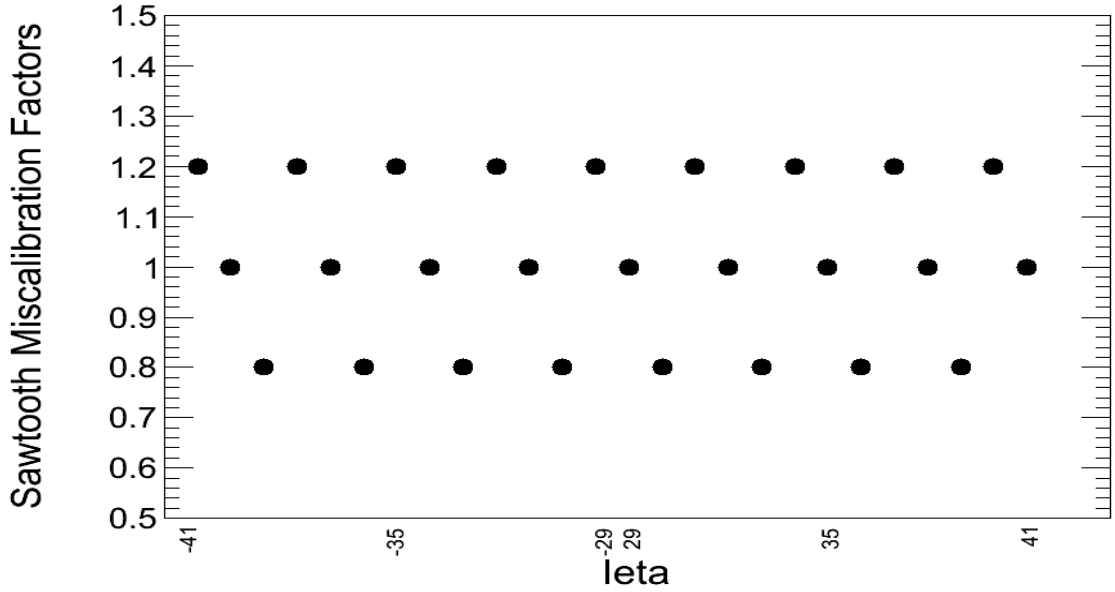

Figure 9: Sawtooth miscalibration scenario

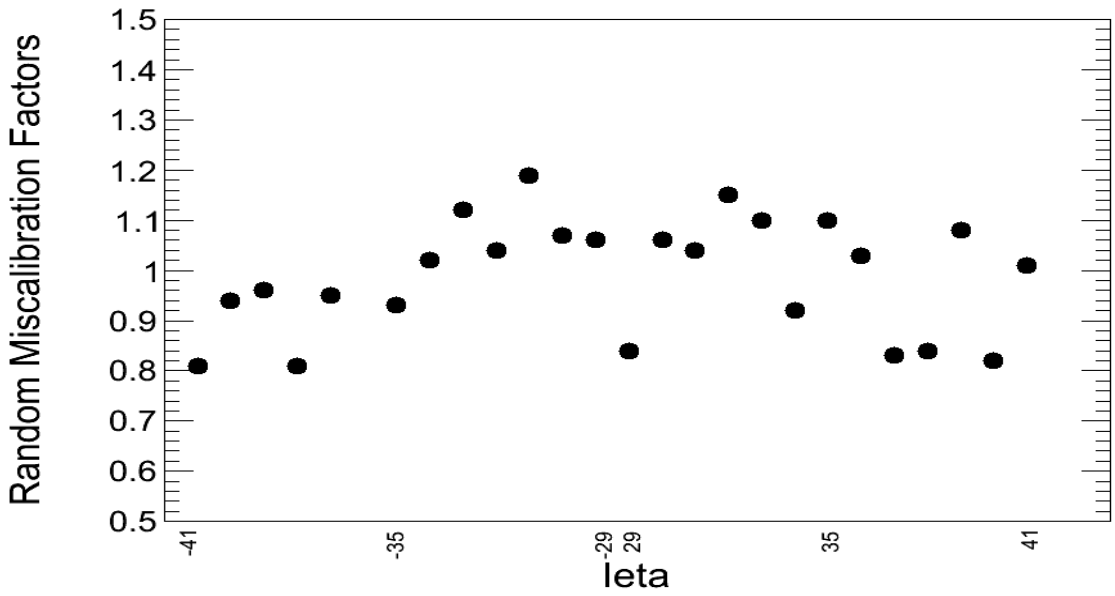

Figure 10: Random miscalibration scenario

$\Delta R < 0.4$ for the HCAL (there is no inner cone for the HCAL). For Z→ee events the recommended upper thresholds for these isolation variables are 5.1 GeV/c for the tracker isolation, 5.0 GeV/c for the ECAL isolation, and 3.4 GeV/c for the HCAL isolation [4] [5]. However, the background can be reduced, albeit simultaneously reducing signal statistics, by employing tighter isolation cuts. For this purpose the recommended cuts for W→eν events are useful: 1.1 GeV/c (tracker isolation), 3.4 (ECAL isolation), 1.3 (HCAL isolation) [5]. One additionally useful variable for cutting on the ECAL electron is the η covariance of the energy deposited, since electromagnetic showers tend to be narrower than hadronic showers. This covariance, $\sigma_{i\eta i\eta}$ is given an upper bound at 0.028 for both types of events [4] [5].

The decision to use either the Z→ee or W→eν recommended cuts will depend on the background. While the tighter W cuts would greatly reduce the background, it would also reduce the signal statistics. The effect on signal statistics is shown in tables 2 and 3 which give, for integrated luminosities of $10\,\mathrm{pb}^{-1}$and $200\,\mathrm{pb}^{-1}$for each set of cuts: the number of generator level Z bosons in the sample, the number of decays to electron-positron pairs where one decay product is detected in ECAL

and one in HF, the number of events which pass ECAL identification cuts, number of events which pass HF identification cuts, and number of events which pass an invariant mass cut (65-110 GeV). Given the known cross section and filter efficiency of a background data sample, the expected background event rate can be calculated. A fit calibration technique can be defined as the fit of a Gaussian function to the ratio of E_{reco}/E_{pred} for each ieta. Obtaining this ratio for the background sample, and weighting the number of events in each bin by the expected background at a certain integrated luminosity, this can be added to the histogram for the signal, giving a signal+background histogram. However, the weighted background bins will, in most cases, not be filled with integer values. A Poisson function can randomly generate an integer value for the background in each bin. A Gaussian can be fit to this histogram for each ieta at a chosen integrated luminosity, from which a mean is found. These means can be listed as a distribution in a histogram to which a Gaussian can be fit. Since these ratios would ideally be one, the RMS of this Gaussian would ideally be close to zero. Therefore, the preferred isolation cuts can be determined by whichever cuts lead to the lower RMS value at some integrated luminosity. Since the signal+background histograms are dependent on randomly selected integer values for background entries, this RMS was calculated for 100 iterations of the described process. At this time, only a small background sample is available, therefore a low integrated luminosity ($10\,\mathrm{pb}^{-1}$) was chosen at which to evaluate these RMS values. It should be noted that the background sample consists of about 48 million events. Yet the probability of background events occuring is very high while the probability of passing all the selection cuts is low. Therefore the size of the background sample at this time is only sufficient for reliable background modelling for integrated luminosities less than $10\,\mathrm{pb}^{-1}$. The results of these studies are shown in figs. 11 and 12. The mean value in this distribution is slightly smaller for the W cuts, so the tighter isolation cuts were chosen to be used for the rest of the analysis.

The identification of the HF electron starts with measuring the ratio of the energy of a hit deposited in a 3x3 $\eta \times \phi$ cluster to the energy deposited in a 5×5 cluster. Since electrons have narrower showers than jets, we set an identification cut where this ratio is larger than some threshold (in this case 0.94). We further identify the HF electron by the shower's $\eta \times \phi$ width by taking the ratio of it's energy in the seed

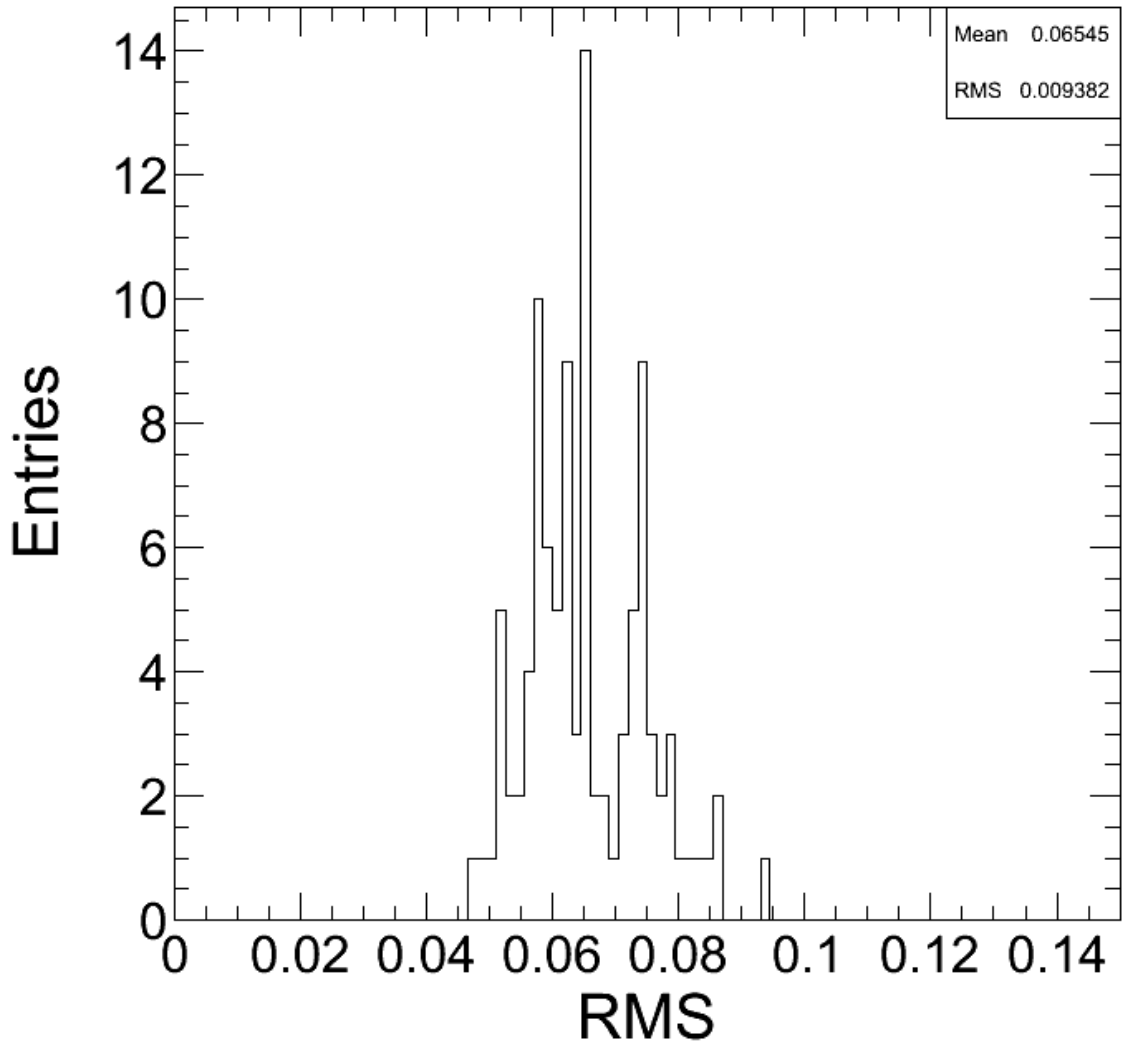

Figure 11: Distribution of RMS values using the recommended isolation cuts for Z→ee events

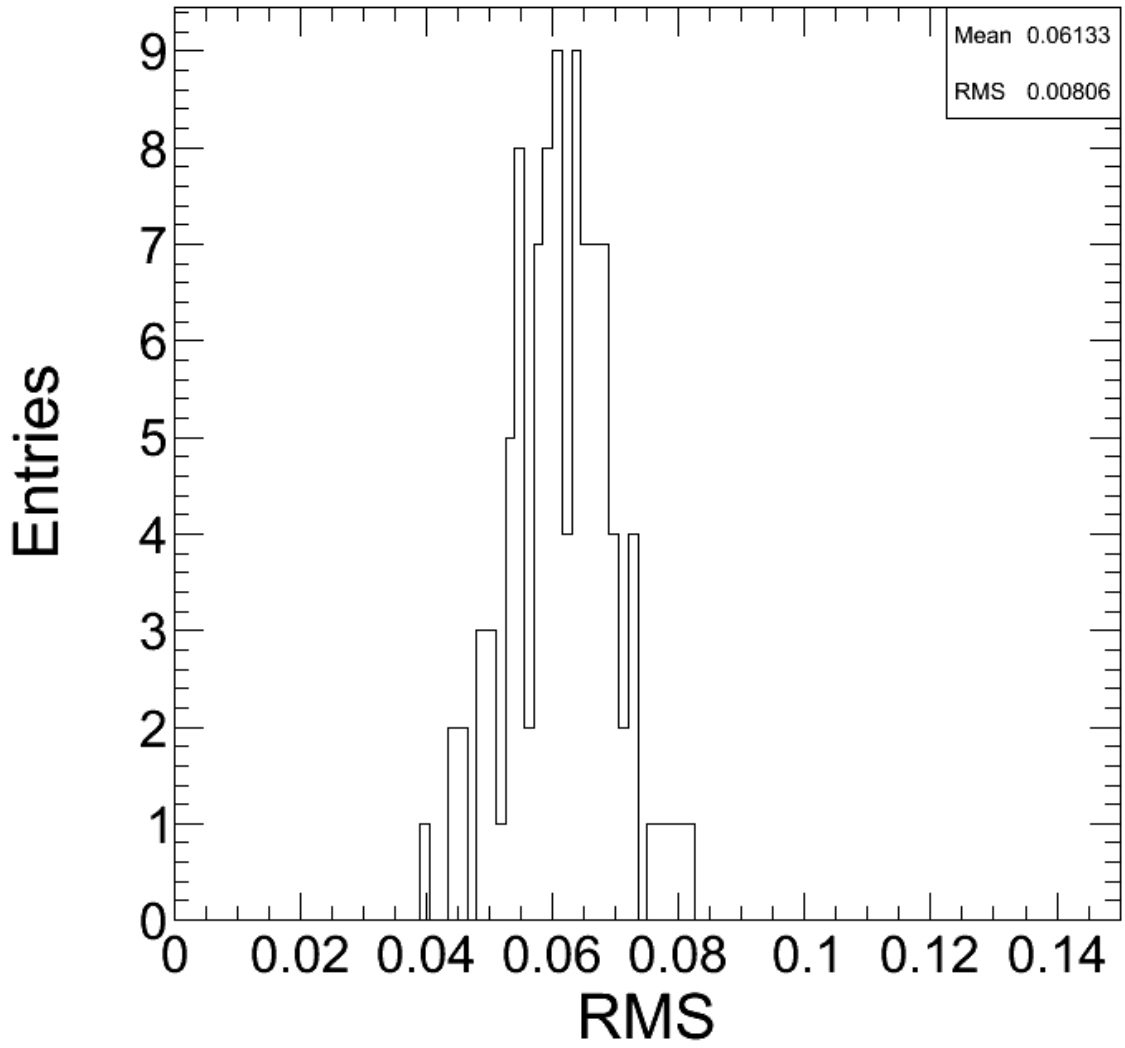

Figure 12: Distribution of RMS values using the recommended isolation cuts for W$\rightarrow$eν events

Table 2: Statistics on number of events passing selection cuts for Z→ee isolation cuts

Selection Cut	$10\,\mathrm{pb}^{-1}$	$200\,\mathrm{pb}^{-1}$
Number of Z Events	12260	236105
Number of ECAL-HF Events	1314	26034
Number Pass ECAL ID Cuts	549	10579
Number Pass HF ID Cuts	537	10437
Number Pass Mass Cut	495	9501

Table 3: Statistics on number of events passing selection cuts for W→eν isolation cuts

Selection Cut	$10\,\mathrm{pb}^{-1}$	$200\,\mathrm{pb}^{-1}$
Number of Z Events	12260	236105
Number of ECAL-HF Events	1314	26034
Number Pass ECAL ID Cuts	470	9155
Number Pass HF ID Cuts	460	9035
Number Pass Mass Cut	424	8217

cell (the cell with the largest fraction of energy deposited) to the energy in the 3×3 cluster and set the cut higher than some threshold. Our final cut has already been mentioned and it is a measure of the ratio of energy deposited in the short fibers to the energy deposited in the long fibers. Obviously, the cut for this variable is taken to be less than some threshold [4].

4.3 Fit Results

The reconstructed and generator level energy of the HF electron is given in each ieta tower, and the distribution of these energies can be graphed individually for each ieta tower. The predicted energy is found from taking the reconstructed position and energy values given for the ECAL electron and the reconstructed position values given for the HF electron and inserting them into the prediction equation for HF electron energy found previously. However, we could perform another analysis using generator level values for either the ECAL or HF electron. The generator level gives true values

for position (ECAL and HF) and energy (ECAL only) and can add a further check on how close the reconstructed energy or a calibration of the reconstructed energy comes to the true value for the energy of the HF electron. This can also be done for events in each individual ieta tower and plotted individually. For each event, we can also take the ratio of E_{reco}/E_{pred}. If the reconstruction is good, the ratio should, ideally, be one for each event.

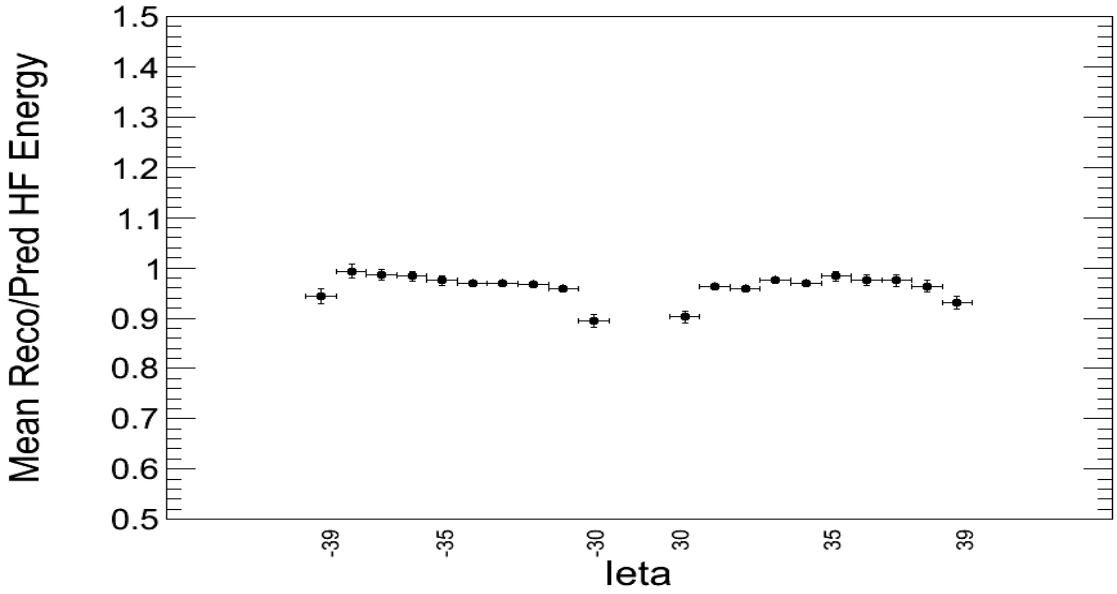

Figure 13: Distribution of mean values of Reco/Pred HF electron energy as a function of ieta in the base case

These ratios can be plotted for each ieta tower to determine the distribution of these ratios. Although the graphs of the distributions of these ratios in each ieta should be centered around one, there will be some width to the distribution. So, we fit a Gaussian function to the distribution and determine the mean from the fit for each ieta tower. These means are then plotted as a function of ieta tower to give us a first approximation in the comparision of predicted and reconstructed energy of the HF electron (see fig. 13).

The next step is to plot the distribution of these means. If the ratio is one for each ieta tower, as we desire, the distribution will just be a peak at one and root mean

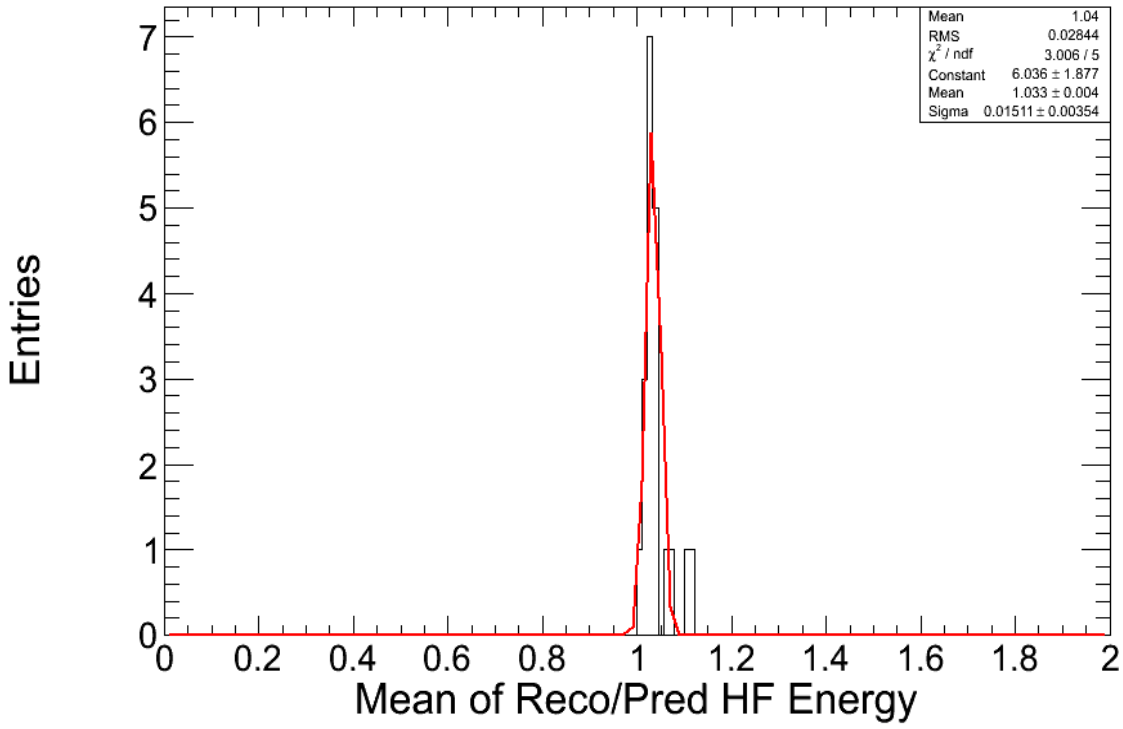

Figure 14: Distribution of the means of HF electron energy for each ieta

square of a Gaussian fitted to this distribution will be zero. So, as a first calibration test, we will check the RMS of a Gaussian fit to this distribution to see how close it is to zero. What's more, this RMS value should decrease as we add more events, so we find how the RMS reduces as we move from integrated luminosities of $4\,\mathrm{pb}^{-1}$to $10\,\mathrm{pb}^{-1}$to $50\,\mathrm{pb}^{-1}$to $100\,\mathrm{pb}^{-1}$to $200\,\mathrm{pb}^{-1}$. Presumably, the best fit is found at the highest integrated luminosities, so our first calibration constant for each ieta tower can be found by taking the inverse of the mean of the reco/pred HF energy for each ieta as found at $200\,\mathrm{pb}^{-1}$. If we multiply this first calibration constant by the ratio of reconstructed to predicted HF electron energy, we can again plot the means of Gaussian fits to these distributions as done previously and again find the RMS values of the distributions of these means, which should be even closer to zero.

However, we could also perform another analysis using generator level values for either the ECAL or HF electron. This can add a further check on how close the reconstructed energy or a calibration of the reconstructed energy comes to the true value for the energy of the HF electron. What's more, a comparison of the RMS values achieved using truth values for the ECAL electron or the HF electron gives us insight into which electron's reconstructed variables are farther from truth values. For example, using the generator level values for the ECAL electron doesn't change the RMS values significantly, which is what we would expect given the position and energy resolution of the crystal calorimeter in the ECAL. However, using the generator level values of the position of the HF electron leads to a significant difference in the RMS values from simply using reconstructed values. As expected, the position resolution is not as good in the HF, which affects the predicted HF electron energy, leading to the larger deviations.

So far, we have only considered the base case where there is no artificial miscalibration of the reconstructed energies of the HF electron. When we introduce the miscalibration scenarios as explained in the previous section, we expect the ratio of reconstructed to predicted HF electron energy to scale as the miscalibration factor. The method for finding a calibration using miscalibration scenarios is mostly analogous to the calibration for the base case. As in the base case, we plot the ratio of the reconstructed (in this case multiplied by the miscalibration factor for its corresponding ieta tower) to predicted energies of the HF electrons as a distribution in each ieta tower

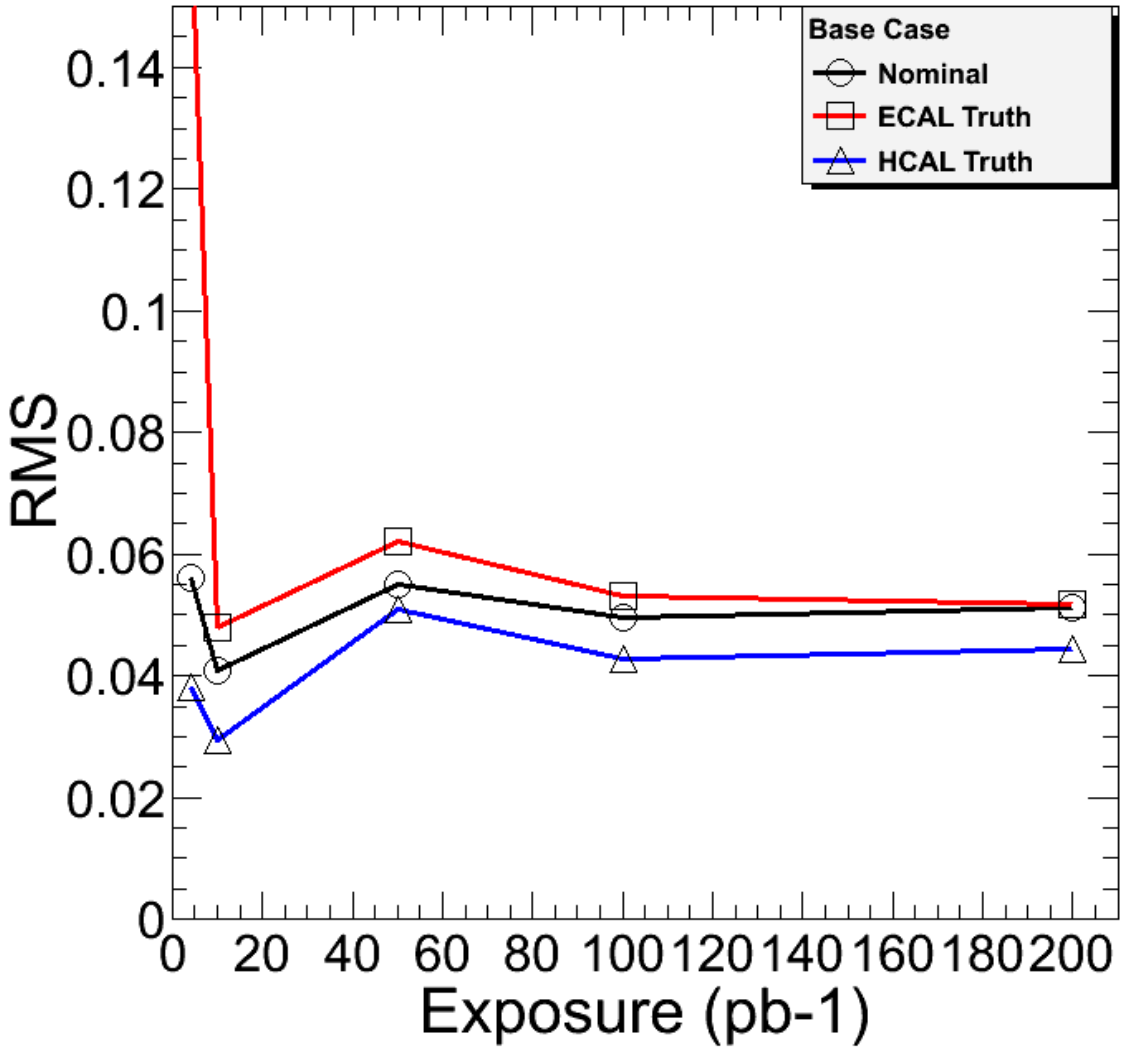

Figure 15: Fit technique RMS values of the distribution of mean values of Reco/Pred HF electron energy over all ietas as a function of luminosity

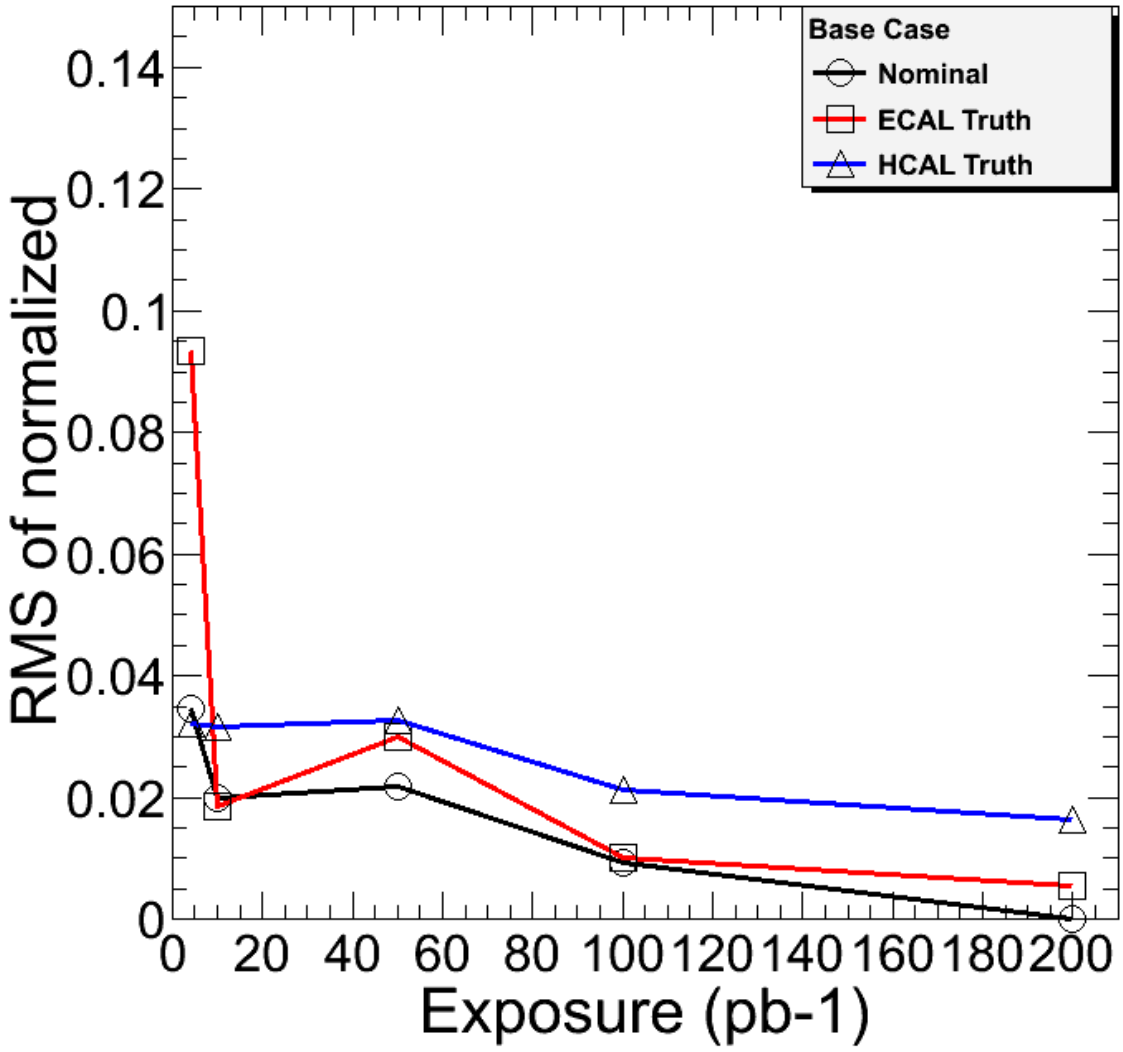

Figure 16: Fit technique RMS values normalized to the mean values for the base case at the luminosity of $200\,\mathrm{pb}^{-1}$

and fit this distribution to a Gaussian, determining the mean of this distribution. We then plot these means as a function of ieta. Unlike the base case, when dealing with miscalibration scenarios we then divide these means by the miscalibration factor we introduced in the beginning and then plot these new means as a function of ieta. The reason for this is, ideally, these new ratios should be one and when plotting the distribution of these means, we should get a peak at one. Realistically, we will find a distribution of means around one and fitting a Gaussian to this distribution, we can find the RMS and plot these root mean squares as a function of integrated luminosity, again ranging from $4\,\mathrm{pb}^{-1}$to $200\,\mathrm{pb}^{-1}$. New calibration constants for each ieta tower in each miscalibration scenario can be found by finding the reciprocals of these new means for each ieta tower at $200\,\mathrm{pb}^{-1}$. This is a valid approach because the difference between E_{reco} and E_{pred} is due to material effects between the interaction point where the HF electron will have energy, E_{pred} and the end of the detector where the measured energy is E_{reco}. See figs. 17 to 21 for normalized RMS values.

4.4 Matrix Results

Recall from Section 3.7 that the calibration constants for each ieta channel can theoretically be found using a matrix calibration technique where the vector $\vec{C}$ representing the calibration constants is set equal to the inverse of a matrix M multiplied by a vector $\vec{b}$. When an electron deposits energy in the HF it does not typically desposit all of its energy in one ieta tower, which is why the matrix technique is designed with the ability to find the amount of energy deposited in each ieta tower for each electron that deposits energy in the HF. Realistically, this is not necessary because the electron will deposit the majority of its energy in one ieta tower, which we will call the seed cell, and the rest can be accounted for by looking at the nearest adjacent ieta tower on either side of the seed cell. Therefore, for every event, A_j or A_i in equations 31 and 32 will have one of three possible values corresponding to the reconstructed energy of the HF electron in either of the three ieta towers considered for that event, with the seed cell containing the largest portion of the total reconstructed energy. Clearly, when we sum over all events in our sample, the matrix M is symmetric with off-diagonal elements of zero far from the diagonal, and small off-diagonal elements

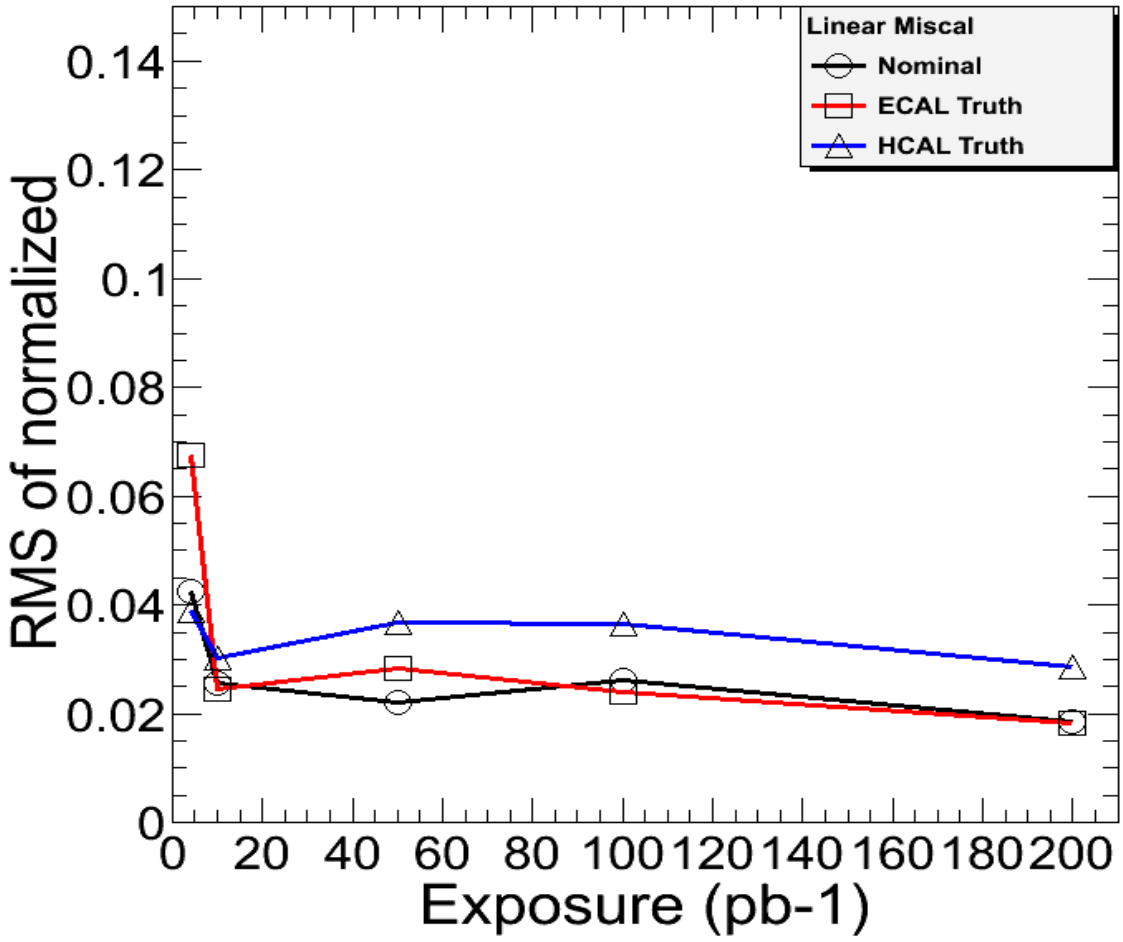

Figure 17: Fit technique RMS values for linear miscalibration normalized to the mean values for the base case at the luminosity of $200\,\mathrm{pb}^{-1}$

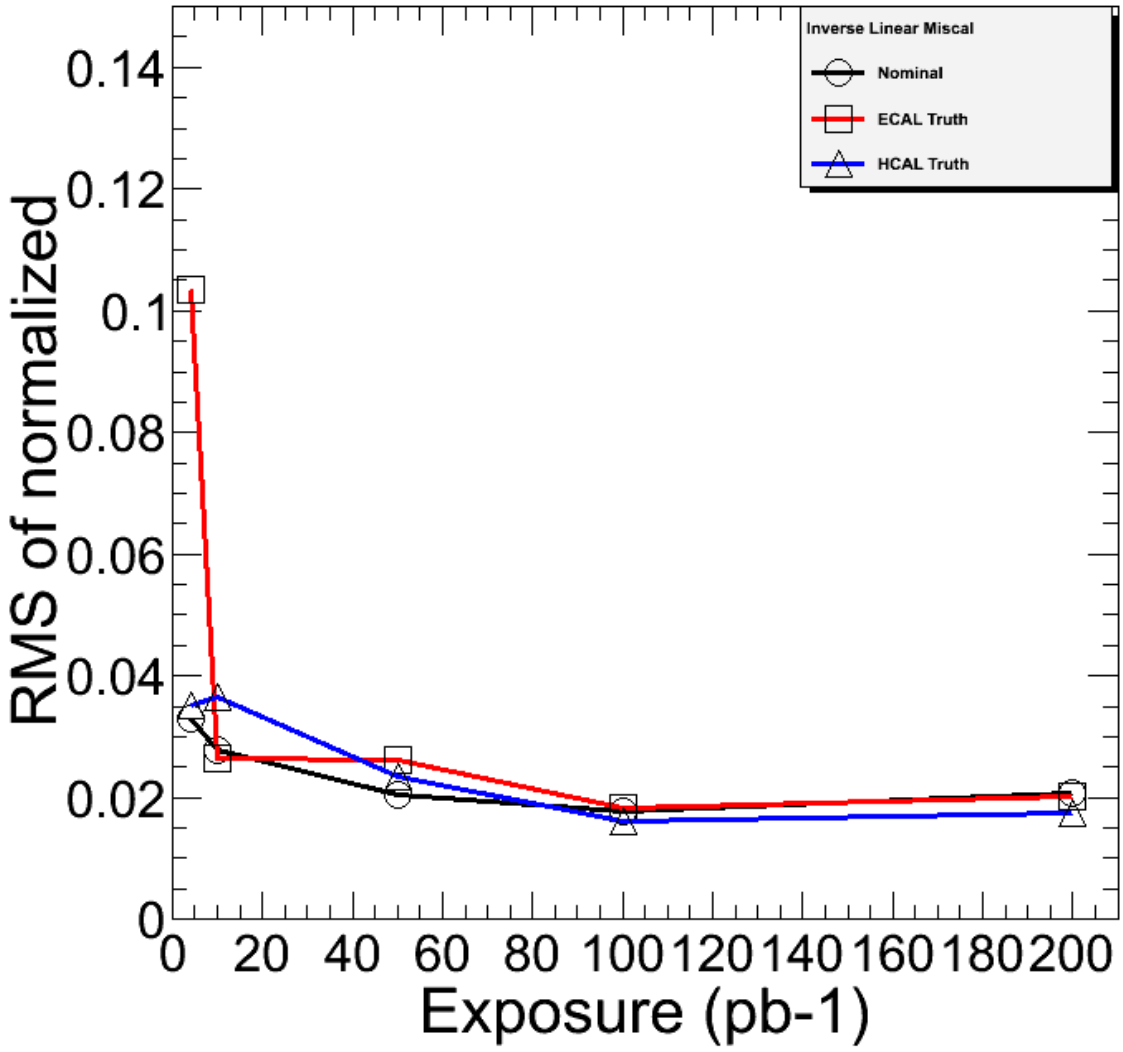

Figure 18: Fit technique RMS values for inverse linear miscalibration normalized to the mean values for the base case at the luminosity of $200\,\mathrm{pb}^{-1}$

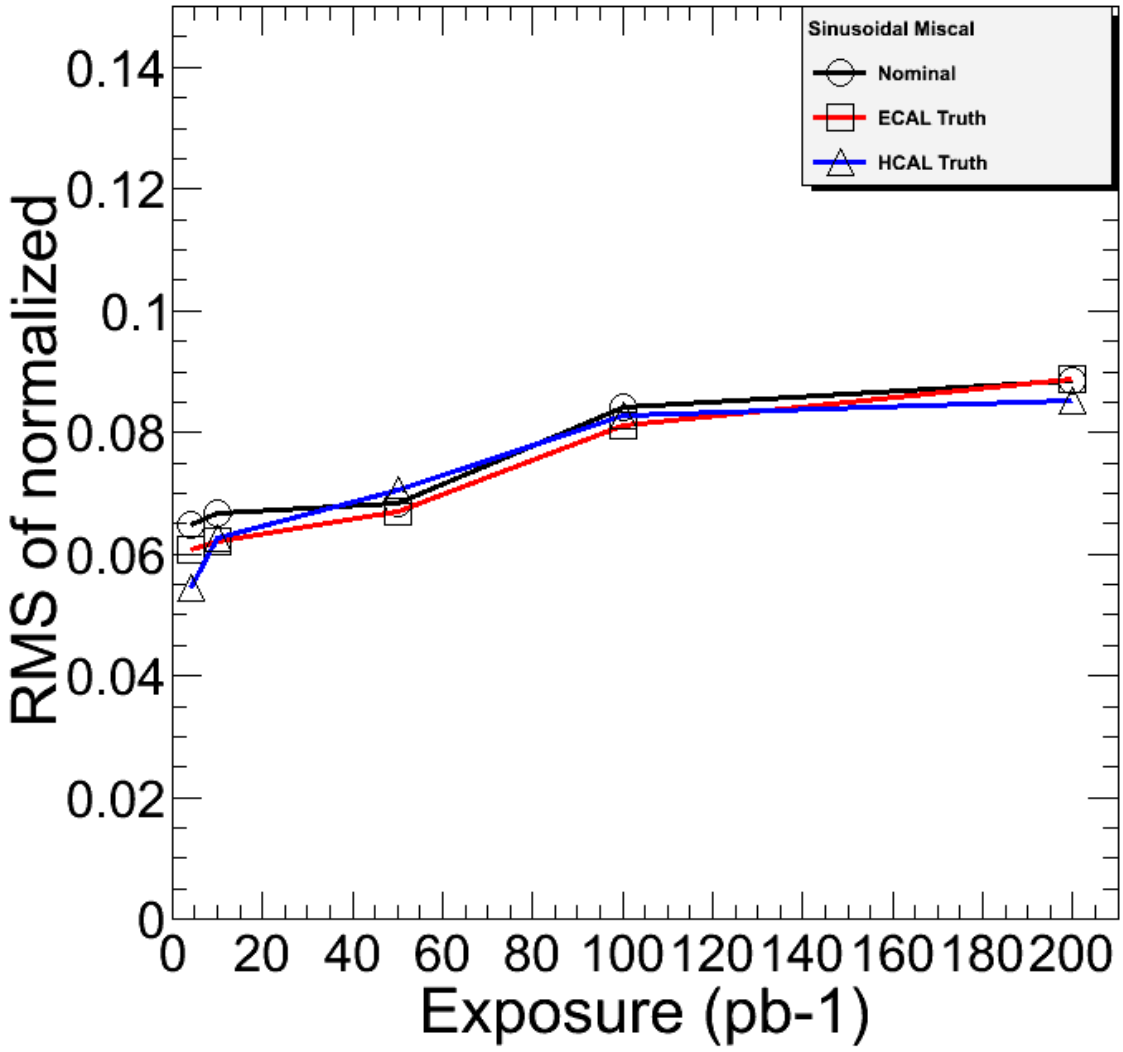

Figure 19: Fit technique RMS values for sinusoidal miscalibrationnormalized to the mean values for the base case at the luminosity of $200\,\mathrm{pb}^{-1}$

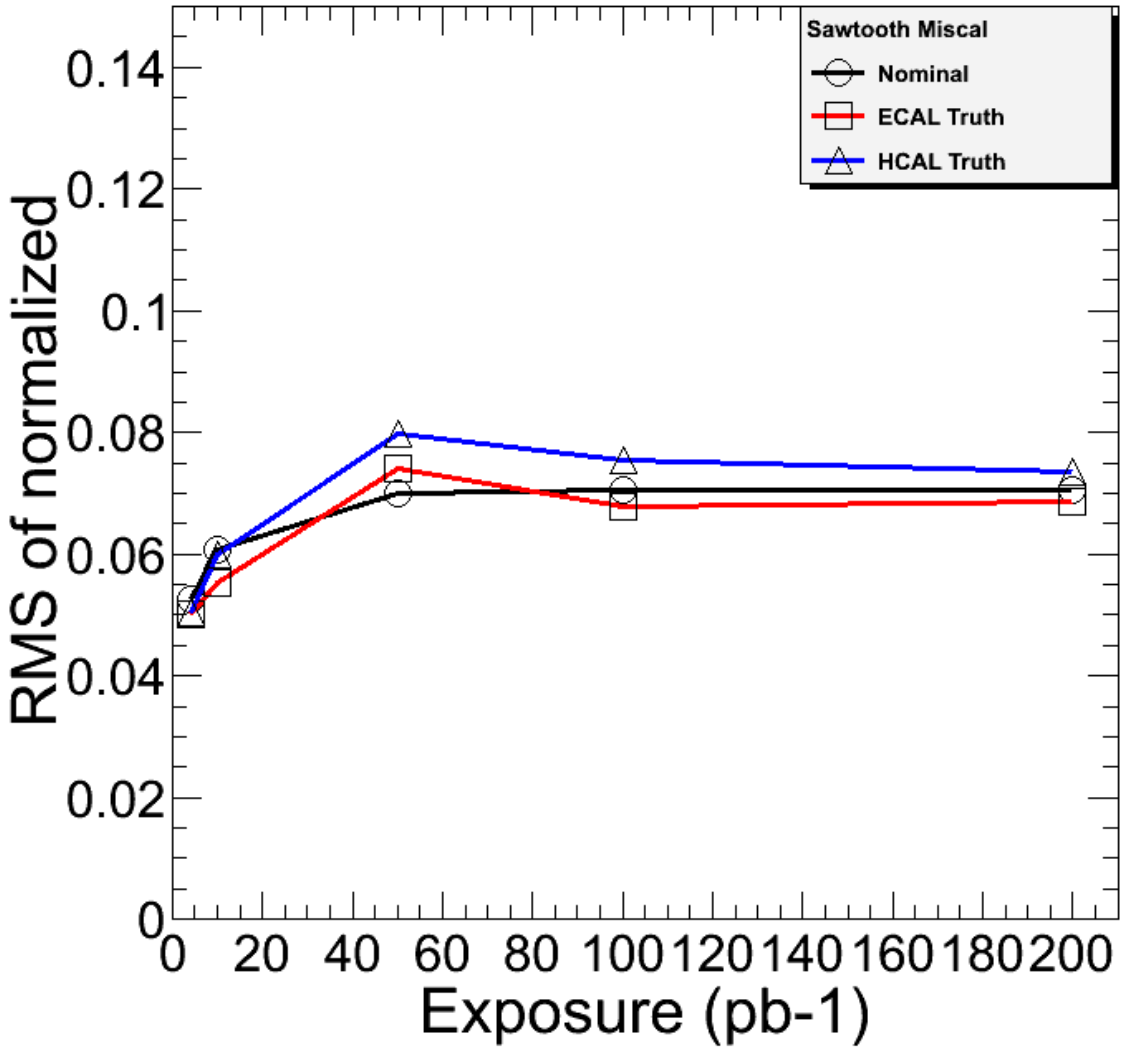

Figure 20: Fit technique RMS values for sawtooth miscalibration normalized to the mean values for the base case at the luminosity of $200\,\mathrm{pb}^{-1}$

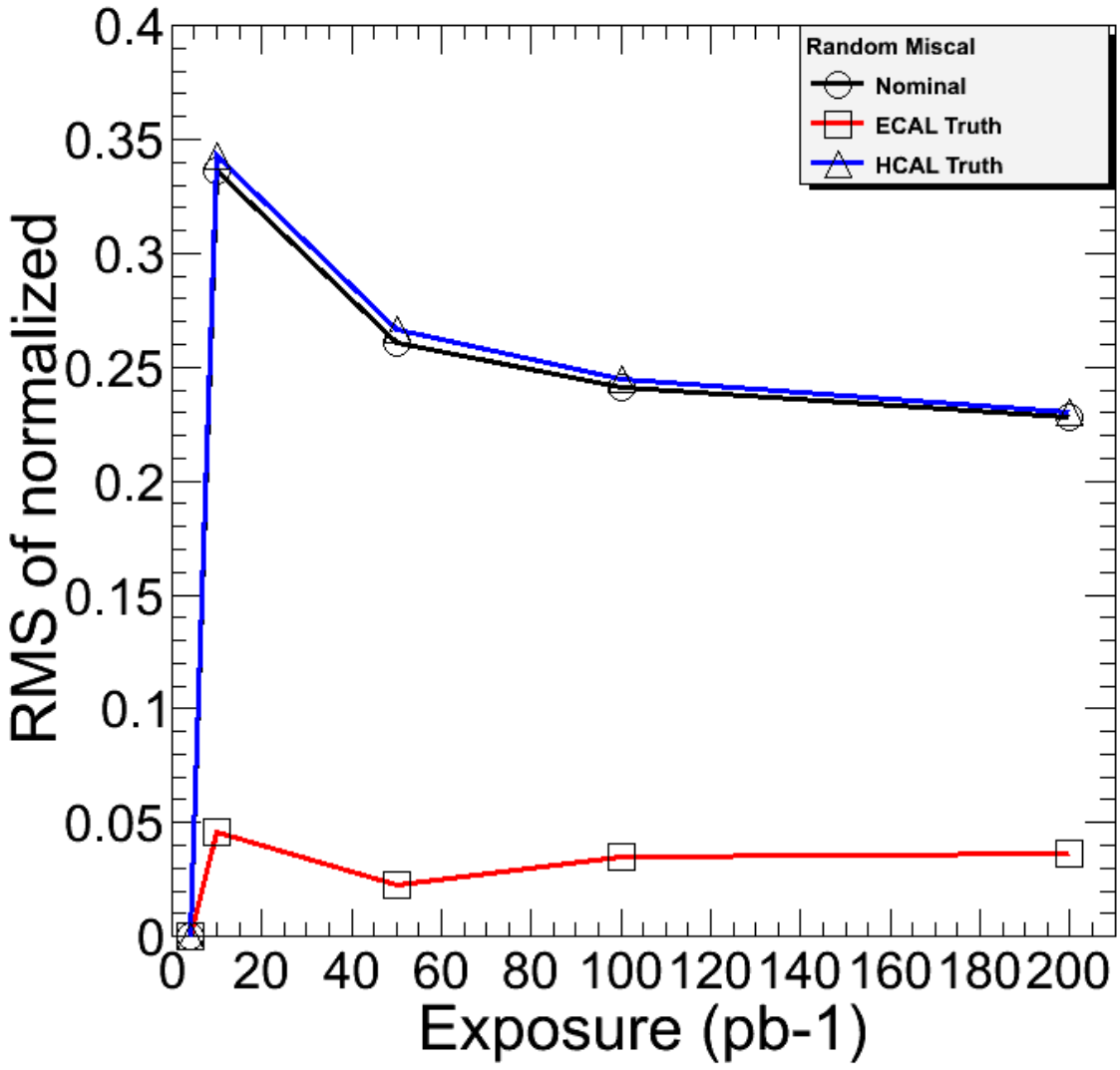

Figure 21: Fit techniqueRMS values for random miscalibration normalized to the mean values for the base case at the luminosity of $200\,\mathrm{pb}^{-1}$. Note the change in vertical scale.

(relative to the diagonal elements) adjacent to the diagonal. The vector $\vec{b}$ is likewise found by taking the sum over all events. Taking the inverse of M and multiplying M^{-1} and $\vec{b}$ as in equation 36, yields the vector $\vec{C}$ which gives calibration constants for each ieta channel.

We can evaluate the quality of this calibration in the same way that we evaluated the fit results. The calibration constants can be plotted versus ieta. We can also plot the distribution of these calibration constants. If no further calibration was necessary, we would expect the constants to all be one, which would result in a peak in this distribution at one with an RMS of zero. Again, we will take the RMS value to be an indicator of the quality of our calibration. From our calibration constant distribution, we find the RMS of the Gaussian fit and plot this RMS for each luminosity in our range from $4\,\mathrm{pb}^{-1}$to $200\,\mathrm{pb}^{-1}$. Since we expect the RMS values to gradually decrease as we accept more events, we can normalize our calibration constants for all luminosities to their values at $200\,\mathrm{pb}^{-1}$to bring our RMS values even closer to zero (obviously, in this case the RMS at $200\,\mathrm{pb}^{-1}$will be zero).

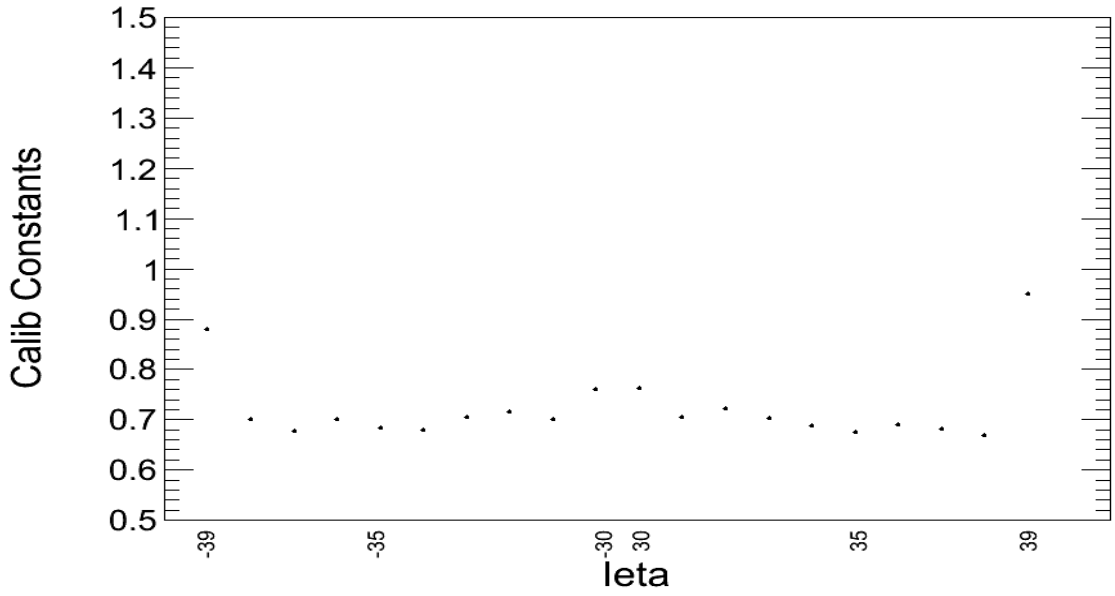

Figure 22: Distribution of calibration constants as a function of ieta found using the matrix technique

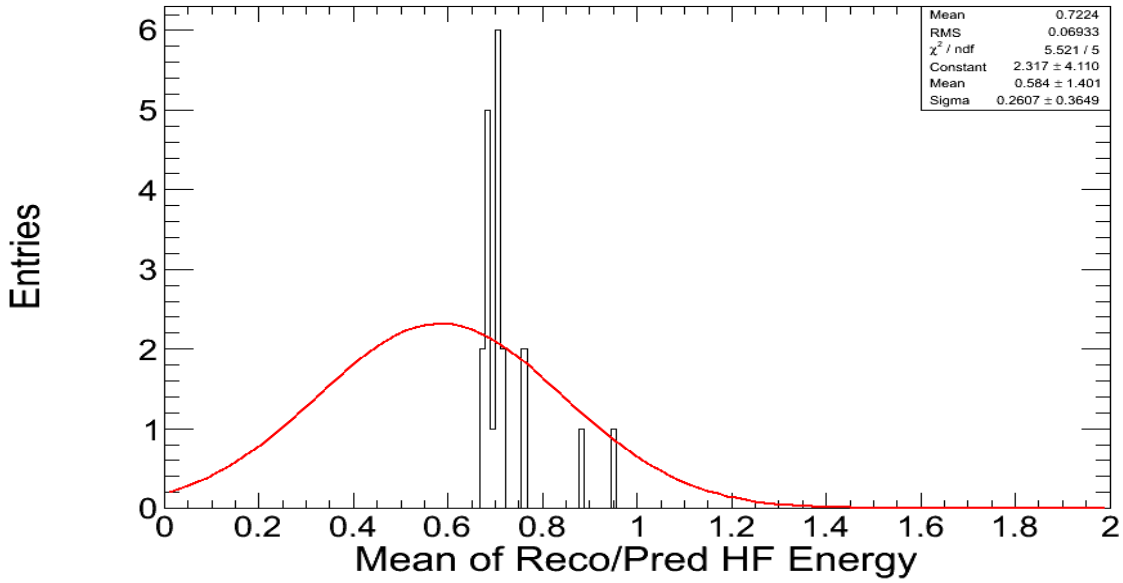

Figure 23: Distribution of calibration constants

When the miscalibration scenarios are applied to the ieta towers, we expect to see calibration constants for each ieta tower that are simply the inverse of the miscalibration factor applied to each ieta tower. Therefore, if no further calibration is necessary, the product of calibration constant and miscalibration factor should ideally be one for each ieta tower. Again, we plot the distribution of this product against ieta, and plot the distribution of these products, finding the RMS of the Gaussian fit to the distribution for each luminosity in our range. And, similarly to the base case, we normalize these products by their values at $200\,\mathrm{pb}^{-1}$for the base case, leading to RMS values closer to zero.

For the base case as well as the miscalibration scenarios, this process can be iterated, theoretically leading to a succession of calibration constants which are closer and closer to one.

4.5 Conclusions

With no miscalibrations applied, the fit technique gives a smaller RMS for the mean values of E_{reco}/E_{pred} ($\sim 5\%$) than the matrix technique ($\sim 7\%$) at luminosities of

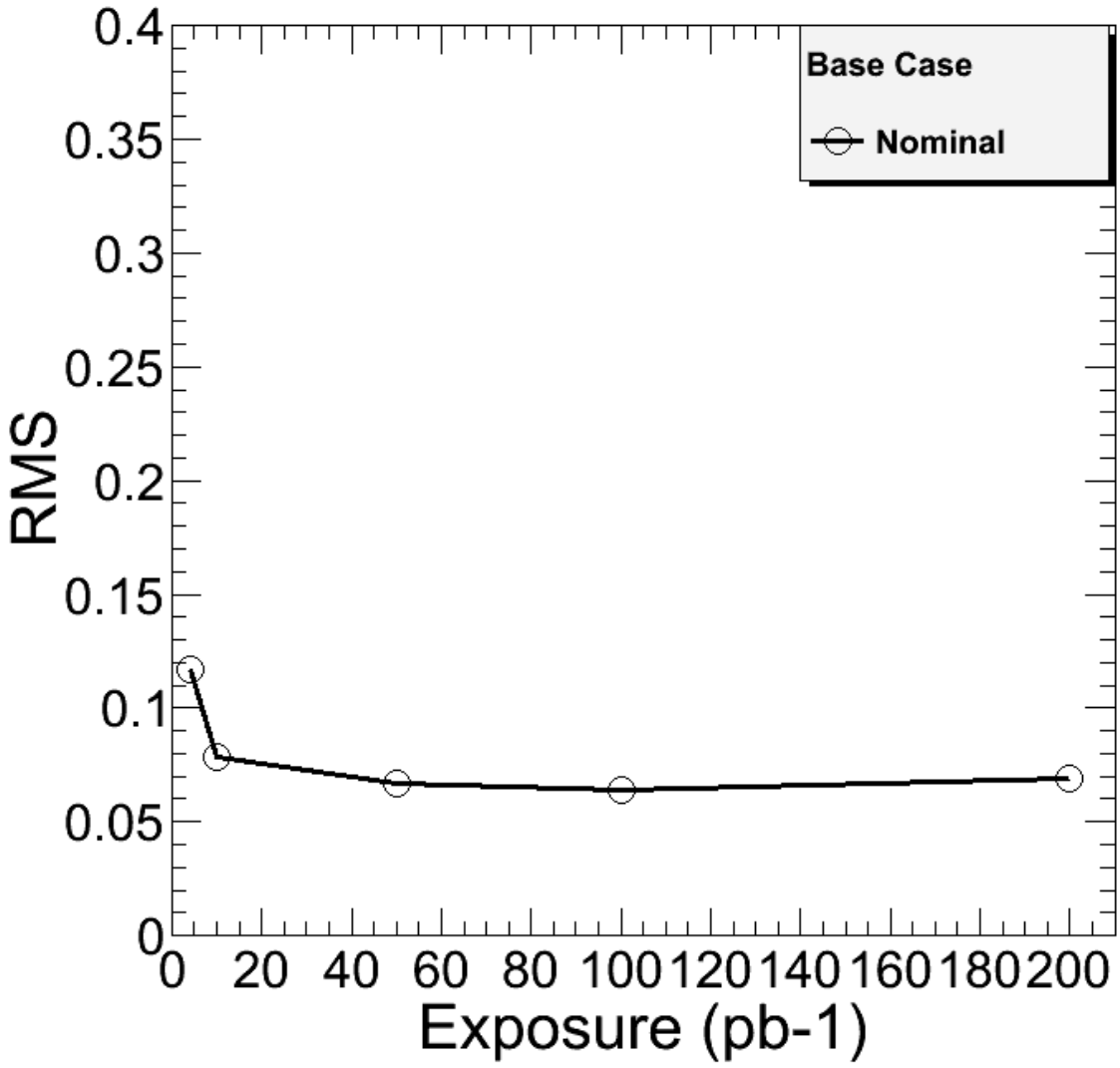

Figure 24: Matrix techniqueRMS values of distribution of calibration constants found using the matrix technique as a function of luminosity

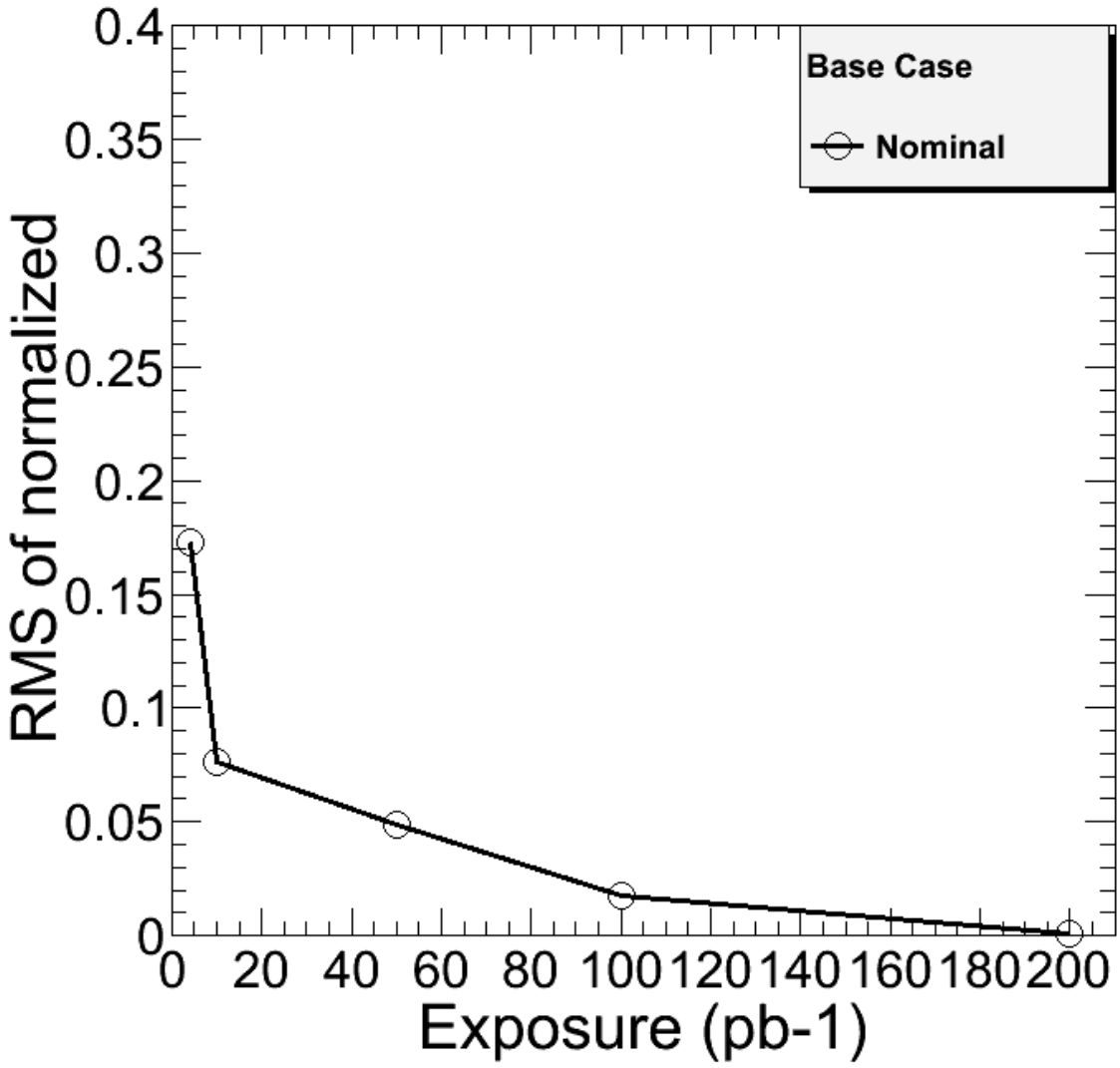

Figure 25: Matrix technique RMS values of distribution of calibration constants normalized to the values of the base case at luminosity $200\,\mathrm{pb}^{-1}$

$200\,\mathrm{pb}^{-1}$. Likewise, for the first miscalibration scenario (linear miscalibration) the fit technique gives a smaller RMS value at $200\,\mathrm{pb}^{-1}$than the matrix technique (4% compared to 7%). However, when the means are normalized to their values in the base case at $200\,\mathrm{pb}^{-1}$, the RMS values of these normalized means in both the fit and matrix technique are $\sim 2\%$ at $200\,\mathrm{pb}^{-1}$. We get similar results for the inverse linear miscalibration scenario. Interestingly, as we move to the sinusoidal miscalibration scenario, the RMS values at $200\,\mathrm{pb}^{-1}$are higher for the fit technique than the matrix technique (compare $\sim$ 9.5% to $\sim$ 8%), and the differences in RMS values of the normalized means at $200\,\mathrm{pb}^{-1}$are even more pronounced ($\sim 9\%$ in the fit to $\sim 6.5\%$ in the matrix). The sawtooth miscalibration scenario yields smaller RMS values at $200\,\mathrm{pb}^{-1}$for the fit technique than the matrix technique ($\sim$ 5.5% compared to 7%). However, the RMS values of the normalized means actually increase for the fit technique while decreasing in the matrix technique (compare $\sim 7.5\%$ to $\sim 5\%$). The random miscalibration scenario gives the largest RMS values of any miscalibration scenario in either technique, but especially for the normalized case in the fit technique. While the RMS values of the unnormalized and normalized means in the matrix technique change from 12% to 13% the values for the fit technique change from around 7% to 23% at $200\,\mathrm{pb}^{-1}$.

These results seem to indicate that for channel-to-channel correlations in ieta that correspond to random miscalibrations, a matrix technique would be more useful if the goal is to achieve agreement with a non-miscalibrated base case. Since the purpose of introducing miscalibration scenarios was to stress test our calibration against any artifical miscalibrations in the detector, the results from the miscalibration scenarios should, ultimately be compared to the results achieved in the base case. This favors the RMS results from the normalized means which do not significant differ for either fit or matrix technique for linear or inverse linear miscalibrations, but slightly favor the matrix technique for the rapidly fluctuating sinusoidal and sawtooth miscalibration scenarios. The noteable exception is in the random miscalibration scenario which highly favors the matrix technique.

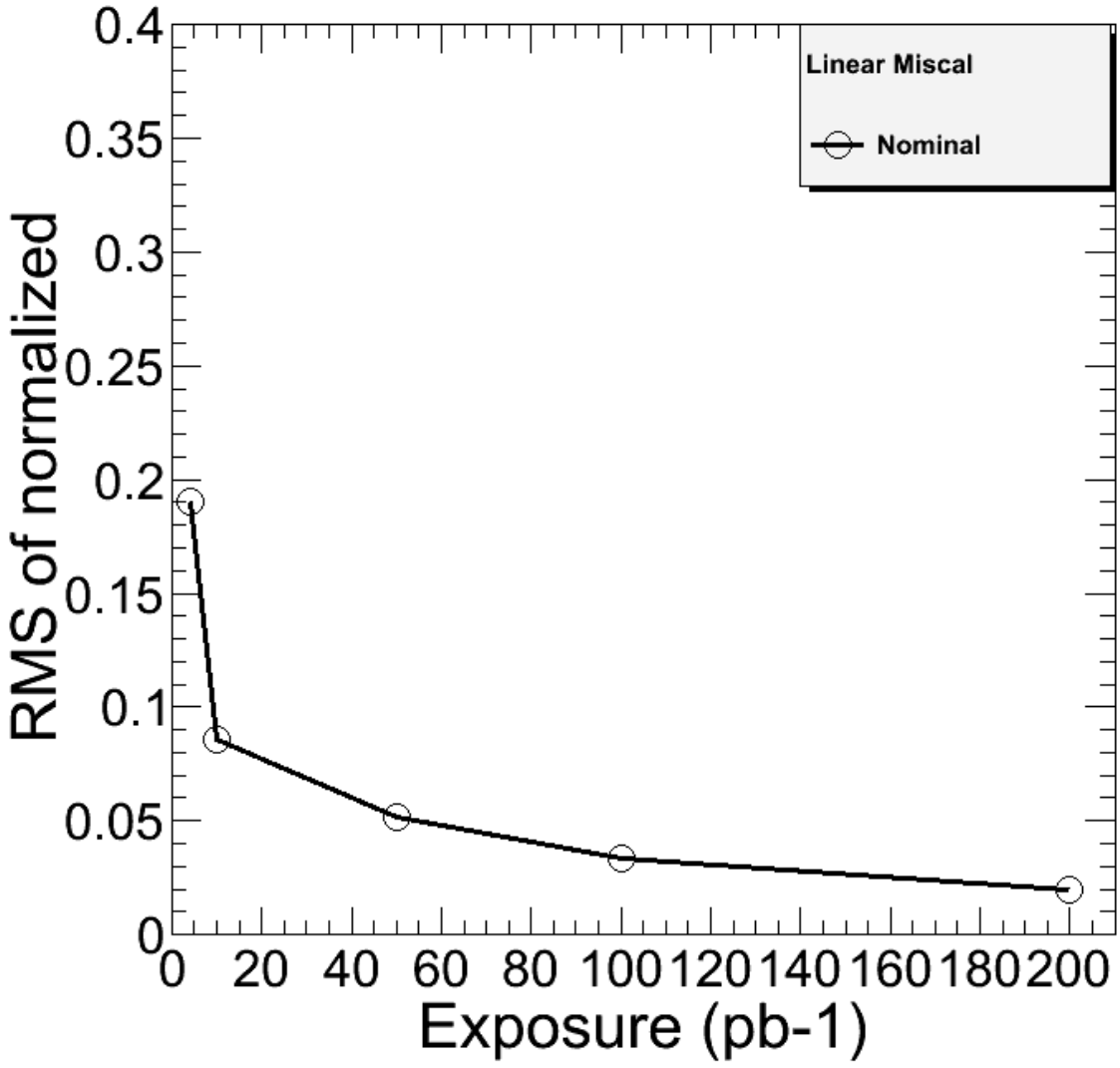

Figure 26: Matrix technique RMS values of distribution of calibration constants in linear miscalibration scenario normalized to the values of the base case at luminosity $200\,\mathrm{pb}^{-1}$

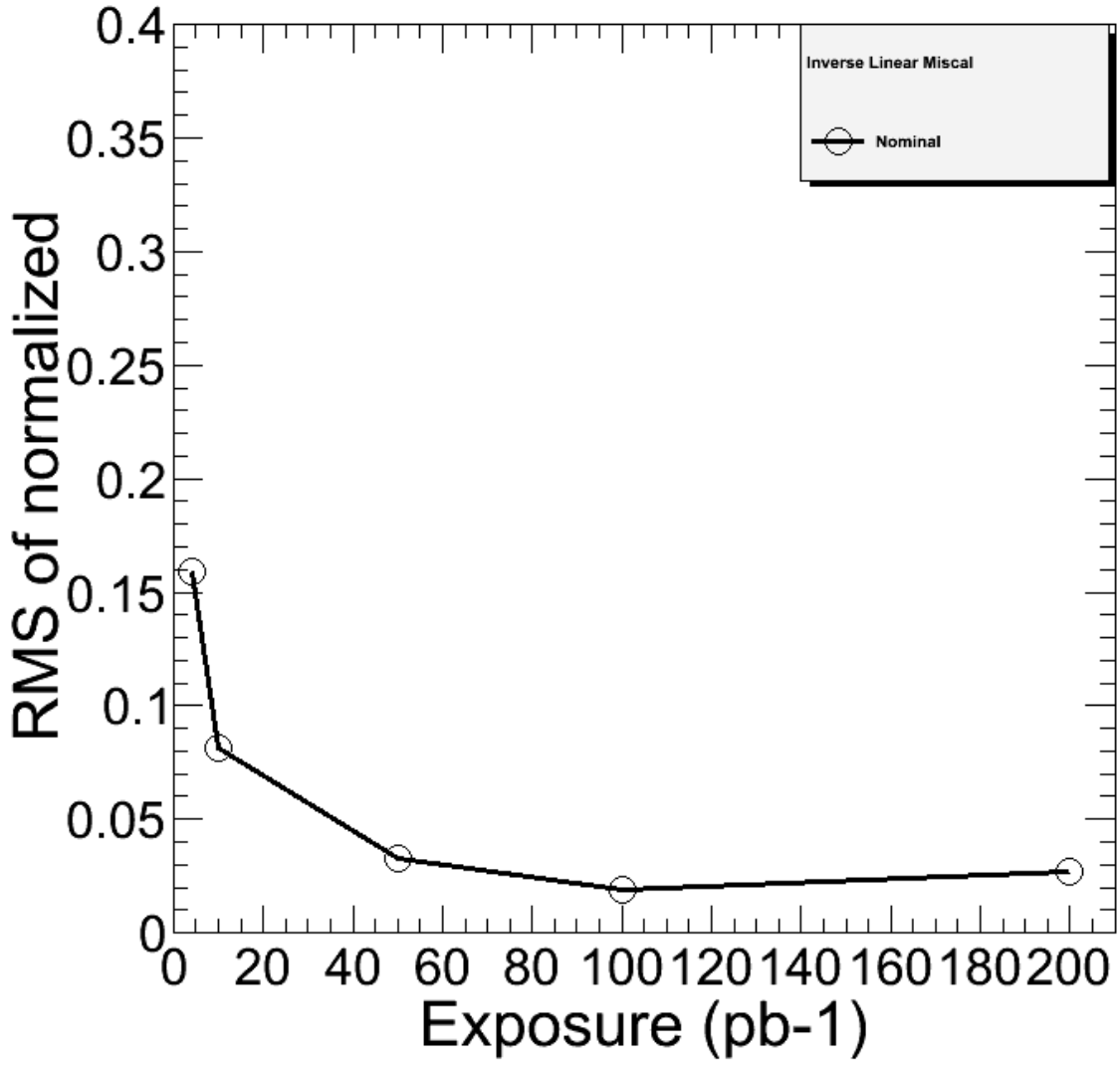

Figure 27: Matrix technique RMS values of distribution of calibration constants in inverse linear miscalibration scenario normalized to the values of the base case at luminosity $200\,\mathrm{pb}^{-1}$

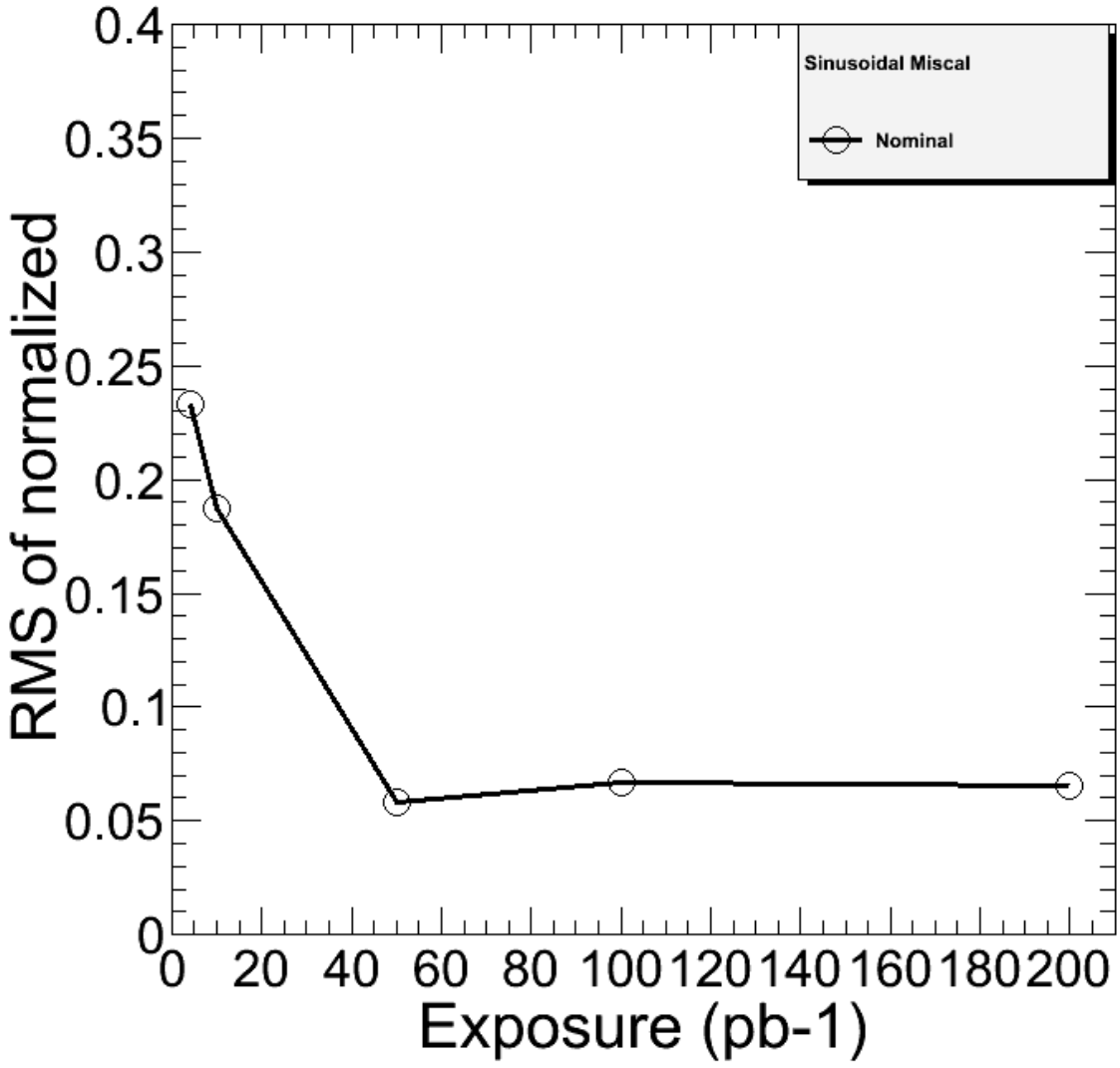

Figure 28: Matrix technique RMS values of distribution of calibration constants in sinusoidal miscalibration scenario normalized to the values of the base case at luminosity $200\,\mathrm{pb}^{-1}$

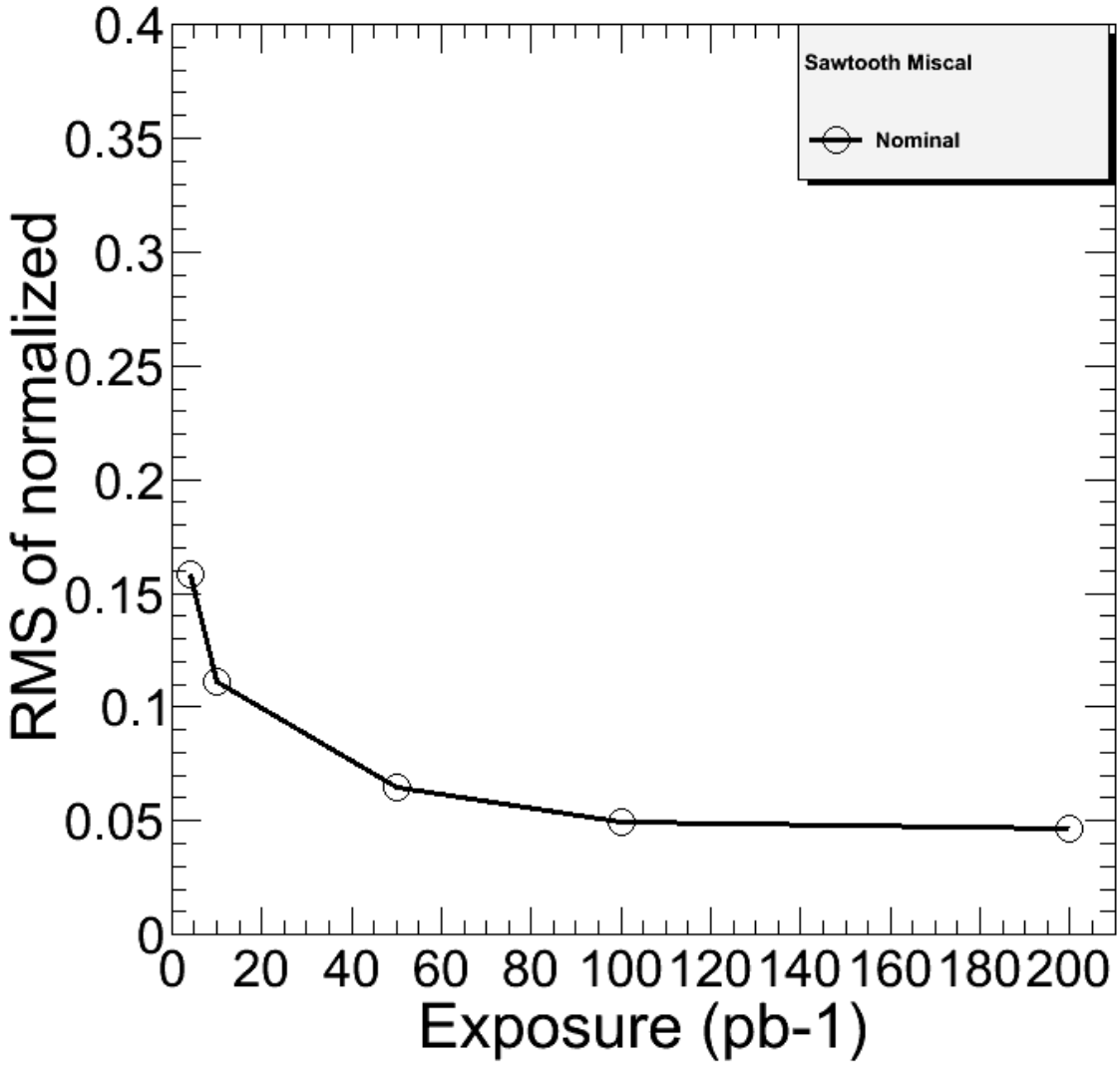

Figure 29: Matrix technique RMS values of distribution of calibration constants in sawtooth miscalibration scenario normalized to the values of the base case at luminosity $200\,\mathrm{pb}^{-1}$

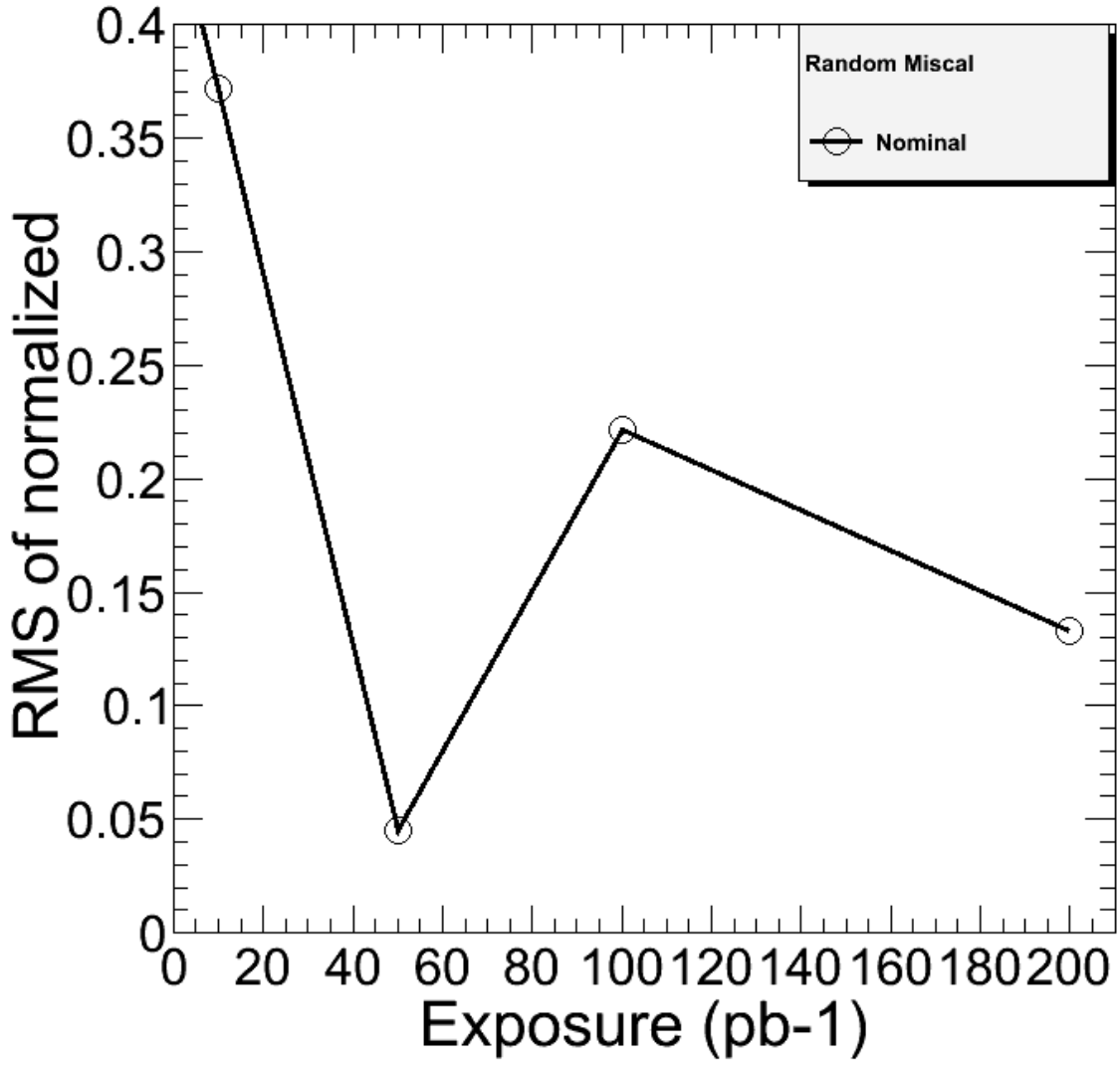

Figure 30: Matrix technique RMS values of distribution of calibration constants in random miscalibration scenario normalized to the values of the base case at luminosity $200\,\mathrm{pb}^{-1}$

5 Conclusion

This paper has presented the preliminary results of fit and matrix calibration techniques which may be employed in the energy calibration of the HF. The use of artificially applied miscalibration scenarios as a means to stress test any calibration technique has also been explained and justified. The application of both calibration techniques to the base case as well as the five miscalibration scenarios indicate that when the goal is to achieve agreement with the base case at an integrated luminosity of $200\,\mathrm{pb}^{-1}$, a goal which has been justified in this paper, linear or inverse linear miscalibrations in ieta yield similar results. Yet for sinusoidal, sawtooth, and especially random miscalibrations, the matrix technique has been shown to be preferrable to the fit technique.

As noted in the discussion of the background sample, the size of the current background sample is not sufficient for effective background modelling for integrated luminosities above $10\,\mathrm{pb}^{-1}$. Future work in this area will have to be done to more fully understand the effects of the background with a larger background sample; however, such a dataset does not currently exist.

References

[1] D. Acosta et al., *CMS Physics:Technical Design Report*, "Technical Design Report"

[2] *Design, Performance and Calibration of CMS Forward Calorimeter Wedges*, G. Baiatian, A. Sirunyan et al., "Eur. Phys. J. C53:139-166, (2008)".

[3] C. Amsler et al. (Particle Data Group), "Physics Letters B667, 1 (2008)"

[4] B.Dahmes, P. Dudero et al., *Measurement of the Shape of the Boson Rapidity Distribution for pp→ Z/gamma*→e+e-+X Produced at* $\sqrt{s}$ *of 10 TeV*, "CMS Analysis Note, (2009)"

[5] N. Adam, J. Berryhill et al., *Towards a Measurement of the Inclusive W→eν and* $\gamma/Z\rightarrow e^+e^-$ *Cross Sections in pp Collisions at* $\sqrt{s}$*=10 TeV*, "CMS Analysis Note, (2009)"